

---

# 9 Numerical Ice-Sheet Models

## 9.1 INTRODUCTORY REMARKS

The word *model* has a wide range of meanings, but in the context of this chapter, the meaning is restricted to computer code written and developed to simulate flow of glaciers and ice sheets. The primary motivation for developing numerical models of glaciers is to better understand the behavior of glaciers and how they may react to changes in external forcing. These models are commonly based on some fundamental laws or assumptions thought to describe glacier flow. However, these simplifications do not necessarily apply to real ice sheets, and it is therefore of fundamental importance that models are thoroughly evaluated.

When it comes to evaluating model performance, the terminology used by different researchers can be confusing with words such as *verification*, *validation*, and *testing* often used interchangeably. In an attempt to bring some uniformity in terminology, Van der Veen (1999c) and Van der Veen and Payne (2003) propose the four terms *verification*, *validation*, *calibration*, and *confirmation* to describe the different levels of the process of model evaluation. This terminology is to a large extent based on similar discussions in the hydrological sciences (for example, Anderson and Bates, 2001).

Models cannot be verified. The term *verification* implies that the truth of the model has been demonstrated (Oreskes et al., 1994). More formal definitions are given by Ayer (1953) and by Fetzer (1988), who concludes that verification of models that describe open natural systems is “not even a theoretical possibility” (p. 1048). To illustrate this point, consider that ice-sheet models are based on concepts of continuum mechanics with Glen’s flow law providing the relation between applied stress and resulting rate of deformation. This relation is based on laboratory experiments on single ice crystals and small blocks of ice, conducted over time scales that are insignificant compared with the residence time of ice in glaciers and ice sheets. Theoretical considerations provide some constraints on permissible relations between the stress and strain-rate tensors but do not conclusively constrain the flow law. Verification of the flow law, and ice-sheet models in general, would require experimental observations of processes acting on the scale of individual crystals throughout entire ice sheets and throughout their entire history, and without interfering with the flow of the glacier. This is, of course, not a feasible approach. A pragmatic approach to evaluate the veracity of a model is to adopt a two-step procedure involving validation and confirmation, in order to demonstrate that some level of confidence can be placed in model predictions.

Van der Veen and Payne (2003) propose that the term *validation* should be restricted to assessing only the numerical model and to demonstrate that the model does not contain any obvious or detectable flaws. This means that when the conceptual model for the system to be modeled is accepted, predictions of the numerical program should be consistent with this conceptual model. For example, if isothermal lamellar flow along a flowline on a horizontal bed is considered, the numerical model should predict a steady-state profile corresponding to the Vialov profile. Bueler et al. (2005) derive several analytical solutions for the isothermal shallow ice equations and propose a specific suite of tests to validate numerical models (note that these authors use the term *verification* for the process of validation). Another possibility for validating models is conduct model intercomparisons, in which similar models developed by different groups are subjected to benchmark experiments (for example, Pattyn et al., 2008, 2012). Such intercomparisons can bring to light inconsistencies among models that arise from numerical details such as grid spacing and numerical schemes used to solve the governing partial differential equations. For example, Vieli and Payne (2005) compared the ability of different models to simulate grounding-line migration and found that in models using a fixed grid size, grounding-line dynamics are strongly influenced by the discretization scheme used. The implication of this finding is that little confidence can be placed in results obtained with these models. Again, it is important to note here that a successful validation does not, and cannot, make any claims regarding how appropriate the conceptual model is for describing actual processes controlling glacier flow (Van der Veen, 1999c).

After ensuring that the numerical code reliably solves the mathematical equations describing the conceptual physical model, the next step in the evaluation process is to compare predictions of the model with actual observations. Most models contain unknown or poorly constrained parameters whose values can be adjusted to improve or optimize the match between observations and model predictions. This process of parameter tuning is called *calibration* and serves to demonstrate that the model is capable of reproducing observations within a certain range or parameter uncertainty (Anderson and Woessner, 1992). It is important to keep in mind that calibration does not provide any information about how appropriate the model is in describing processes occurring in nature. Rather, it shows that models usually contain enough adjustable parameters to make model predictions match observations.

The final step in the evaluation process is that of *confirmation*, or demonstrating that the model constitutes a realistic description of the physical processes being modeled. This again involves comparing model predictions with additional observations that were not used in the calibration process. Of course, models can never be absolutely confirmed, as this would imply verification of the model. However, following Strahler (1987), a “ladder of excellence” can be envisioned, with each rung representing some level of confidence that can be placed in the model’s ability to describe processes in nature. As the model is confirmed by increasingly more observations, it rises up the ladder. It is important in this respect that model predictions to be tested against observations are not trite or obvious (“if snowfall increases, the ice sheet will grow”). In the words of Popper (1963, p. 112), “Confirmation should only count if they are the result of *risky predictions*.”

More often than not, insufficient data are available to determine whether the conceptual framework on which a particular model is based is correct or not. To illustrate this, consider the study of Nick et al. (2007), who applied a flowline model to simulate advance and retreat of Columbia Glacier, an Alaskan tidewater glacier undergoing rapid retreat since the early 1980s. The conventional view is that retreat will continue until the terminus reaches the head of its fjord, where the bed rises above sea level. Subsequent terminus advance down the fjord where the bed is below sea level is made possible by “conveyor-style” sediment recycling and the formation of a sediment bank at the glacier terminus (Section 8.5). Nick et al. (2007) include two calving criteria, the height-above-buoyancy model and the water-depth relation (c.f. Section 8.5) and find that irrespective of which calving relation is implemented, the model glacier cannot advance into deeper water (~300 m water depth or more) unless sedimentation at the glacier front is included. A later study (Nick et al., 2010) incorporates a different calving criterion (based on crevasse depth; Section 8.5) and finds that this model does allow terminus advance across basal overdeepenings without having to invoke sedimentation near the terminus. In the absence of additional observations or information on, for example, sedimentation rates near the terminus, or calving rates, it is not possible to assess which of these two modeling studies best encapsulates the physical processes controlling advance and retreat of tidewater glaciers.

Models can be separated into two categories, namely, diagnostic and prognostic. A *diagnostic* model describes a certain process such as parameterizations of the surface mass balance, or the relation between depth-averaged ice velocity and driving stress for lamellar flow. A *prognostic* model predicts how a process or quantity evolves with time. The most widely used prognostic equations are the continuity equation from which changes in ice-sheet geometry are calculated, and the thermodynamic equation that allows temperature changes to be estimated. When doing so, the implicit assumption is that the diagnostic equations remain valid as the ice sheet changes shape or climate alters significantly. Because many diagnostic models are tuned to present-day observations only, it is not a priori certain that they may be applied under vastly different conditions. The modeler should therefore conduct sensitivity experiments to investigate how small changes or uncertainties in the diagnostic equations affect the behavior of the model ice sheet. Failing to do so renders any model predictions rather useless. Of course, if the model turns out to be very sensitive to certain parameterizations that are ill tested, predictions are not very useful either, other than in identifying key processes that need to be understood better. Such sensitivity studies are all the more important for complex models that cannot be easily reproduced by others.

Numerical models are used in many different ways. One application is to describe in detail the flow of a glacier, adjusting the model parameters and including different physical processes, to better match model predictions with observations. Another application of numerical models is to test the sensitivity of the model glacier to certain processes and how small changes may affect the model behavior. Such studies usually do not pertain to one glacier in particular but are used to identify and study the nature of possible feedback mechanisms. Finally, numerical models can be used to predict past and future evolution of real ice sheets. While such studies are valuable

in providing some idea about possible responses, it should be realized that very few of these models have been adequately evaluated and confirmed. The usual procedure is to run the numerical model to a steady state that agrees reasonably well with the current observed geometry of the Greenland or Antarctic ice sheets. If agreement is not satisfactory, model parameters (such as the illustrious enhancement factor) are adjusted. In other words, the observations are used to tune the model, which is entirely different from actually testing the model.

The following sections in this chapter introduce the basic concepts of numerical ice-sheet models. The objective is not to discuss the most advanced models in great detail, but rather to provide the necessary background to construct relatively simple models for ice flow that can be used to investigate glacier dynamics.

## 9.2 NUMERICAL METHODS

Solving prognostic equations numerically is a science in itself. Many pitfalls exist that may lead to spurious results or errors becoming infinitely large. This is because continuous functions are discretized on a numerical grid, and derivatives are calculated from these grid values. This procedure introduces rounding errors that may adversely affect the solution. While unstable integration schemes are readily discovered, there are other, more subtle, errors that may go undetected. Many excellent textbooks exist on the numerical solution of partial differential equations (for example, Smith, 1985). In this section only a few of the most important issues applying to finite-difference modeling are briefly discussed.

Only single-valued, finite and continuous functions of horizontal distance,  $x$ , and time,  $t$ , are considered here. In a numerical model, the function values are known at discrete gridpoints, with coordinates  $k\Delta x$  and  $n\Delta t$ , where  $k$  and  $n$  represent (positive) integers. Although not necessary, the horizontal grid spacing,  $\Delta x$ , and time step,  $\Delta t$ , are considered constant. To arrive at expressions for horizontal differences, Taylor series expansion is used. For the ice thickness this expansion gives

$$H(x + \Delta x, t) = H(x, t) + \Delta x \frac{\partial H}{\partial x}(x, t) + \frac{(\Delta x)^2}{2} \frac{\partial^2 H}{\partial x^2} + O((\Delta x)^3), \quad (9.1)$$

and

$$H(x - \Delta x, t) = H(x, t) - \Delta x \frac{\partial H}{\partial x}(x, t) + \frac{(\Delta x)^2}{2} \frac{\partial^2 H}{\partial x^2} + O((\Delta x)^3), \quad (9.2)$$

where  $O((\Delta x)^3)$  represents terms containing the third and higher powers of the horizontal grid spacing. Subtracting both expressions and neglecting higher-order terms gives the first horizontal derivative

$$\frac{\partial H}{\partial x}(x, t) = \frac{H(x + \Delta x, t) - H(x - \Delta x, t)}{2\Delta x}. \quad (9.3)$$

Similarly, adding (9.1) and (9.2) yields an expression for the second derivative

$$\frac{\partial^2 H}{\partial x^2}(x, t) = \frac{H(x + \Delta x, t) - 2H(x, t) + H(x - \Delta x, t)}{(\Delta x)^2}. \quad (9.4)$$

These discretizations of derivatives are so-called central differences, because the derivative at a gridpoint is calculated using values at both neighboring gridpoints. For spatial derivatives, this is the most common discretization. For time integrations, a frequently used scheme is forward differencing

$$\frac{\partial H}{\partial t}(x, t) = \frac{H(x, t + \Delta t) - H(x, t)}{\Delta t}. \quad (9.5)$$

The errors involved in discretizing continuous derivatives can, at least in principle, be reduced to an acceptable level by decreasing the grid spacing,  $\Delta x$ , and time step,  $\Delta t$ . This does not necessarily mean that the numerical scheme will converge on the correct solution. This can best be seen by considering the advection equation.

The continuity equation derived in Section 5.2 is an example of an advection equation. For clarity of the following discussion, the advection velocity,  $U$ , is taken constant in the flow direction, and source terms are neglected (no surface accumulation). This is not a very realistic model for glaciers, but it demonstrates clearly some of the difficulties involved in numerically solving differential equations. Under these assumptions

$$\frac{\partial H}{\partial t} + U \frac{\partial H}{\partial x} = 0, \quad (9.6)$$

describes how the thickness changes as ice is being advected in the  $x$ -direction. The solution can be written as

$$H(x, t) = F(x - Ut), \quad (9.7)$$

subject to the initial condition  $H(x, 0) = F(x)$ . In other words, the solution is constant along lines  $x - Ut = \text{constant}$ . Referring to [Figure 9.1](#), the value of  $H$  at point A is equal to the initial value  $H(x_0, t_0)$ . Now consider the discrete form of the advection equation, using central differencing for the horizontal derivative, and forward differencing for the time integration

$$\frac{H_k^{n+1} - H_k^n}{\Delta t} + U \frac{H_{k+1}^n - H_{k-1}^n}{2\Delta x} = 0. \quad (9.8)$$

For brevity, the following notation is used here

$$H_k^n = H(k \cdot \Delta x, n \cdot \Delta t). \quad (9.9)$$

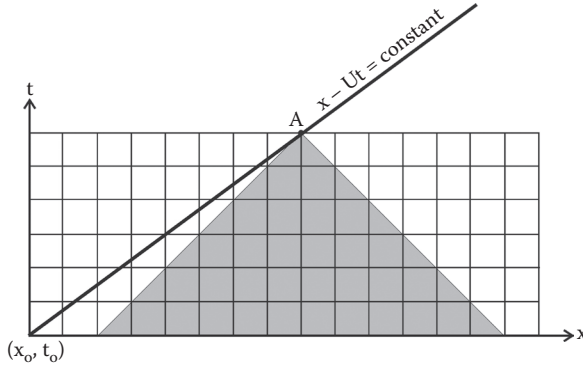


**FIGURE 9.1** Divergence of the numerical solution. The shaded area includes gridpoints whose value affects the calculated result at gridpoint A.

Rewriting equation (9.8) and solving for the new ice thickness gives

$$H_k^{n+1} = H_k^n - \frac{U \Delta t}{2 \Delta x} (H_{k+1}^n - H_{k-1}^n). \quad (9.10)$$

The numerical solution at point A as computed from this equation is determined by the gridpoints falling within the shaded area in Figure 9.1. The gridpoint  $(x_0, t_0)$  falls outside this region and consequently does not affect the calculated value at point A, even though  $H(A) = H(x_0, t_0)$ . Consequently, there is no reason to believe that the numerical solution will converge toward the “true” solution. To ensure convergence, the gridpoint  $(x_0, t_0)$  must fall within the region of points that determine the numerical solution at point A. This is the case if the following criterion is met

$$U \Delta t \leq \Delta x. \quad (9.11)$$

This requirement is the Courant–Friedrichs–Lewy condition, or CFL condition for short.

Another source of error may occur when the numerical scheme is unstable and the numerical solution increasingly diverges from the “true” solution as time integration progresses. This stability can be investigated using the Von Neumann method. The assumption is made that the solution may be written as a Fourier series of harmonic functions and that the stability of each individual Fourier component may be considered separately. Although each harmonic function can be written in terms of sines and cosines, it is more convenient to use the complex exponential formulation. That is

$$H_\omega^n e^{-i\omega k \Delta x}, \quad (9.12)$$

with  $i = \sqrt{-1}$ , represents the Fourier component with frequency  $\omega$ . The change in amplitude of the Fourier component may be written as

$$H_\omega^{n+1} = \lambda H_\omega^n. \quad (9.13)$$

Substituting (9.12) and (9.13) in the discrete form (9.8) of the advection equation gives

$$\lambda - 1 + i \frac{U \Delta t}{2 \Delta x} \sin \Delta x = 0, \quad (9.14)$$

from which the magnitude of the amplification factor,  $\lambda$ , follows

$$|\lambda|^2 = 1 + \left( \frac{U \Delta t}{\Delta x} \right)^2 \sin^2 \Delta x. \quad (9.15)$$

Thus,  $|\lambda|$  is always larger than 1 and the amplitude of the harmonic component will continue to increase with time. The frequency of the Fourier component does not appear in equation (9.15), so that all components continue to grow. In other words, the numerical scheme (9.8) or (9.10) is unstable in the sense that it does not allow a steady solution to be reached.

A numerical scheme that is stable under certain conditions is one in which the time derivative is approximated by forward differencing, and the horizontal derivative by upward (or upstream) differencing

$$\frac{H_k^{n+1} - H_k^n}{\Delta t} + U \frac{H_k^n - H_{k-1}^n}{\Delta x} = 0, \quad (9.16)$$

or

$$H_k^{n+1} = H_k^n - \frac{U \Delta t}{\Delta x} (H_k^n - H_{k-1}^n). \quad (9.17)$$

To evaluate the stability of this numerical scheme, consider again the harmonic component (9.12) with the increase in amplitude given by (9.13). Substitution in equation (9.16) now leads to

$$|\lambda|^2 = 1 - 2 \frac{U \Delta t}{\Delta x} \left( 1 - \frac{U \Delta t}{\Delta x} \right) (1 - \cos(\omega \Delta x)). \quad (9.18)$$

For the solution to be stable, the amplification factor,  $|\lambda|$ , must be one or less. From (9.18) it follows that this criterion is met if

$$\frac{U \Delta t}{\Delta x} \leq 1, \quad (9.19)$$

which is the CFL condition derived earlier.

Having arrived at a numerical scheme that is both convergent and stable, one could proceed with numerically solving the advection equation (9.6). There are more problems looming on the horizon, however. According to equation (9.18), the damping of each harmonic Fourier component depends on its wavelength. This is illustrated in [Figure 9.2](#), which shows  $|\lambda|$  as a function of  $\mu = U \Delta t / \Delta x$ . The decrease in amplitude is largest for  $\mu = 0.5$  and increases as the wavelength

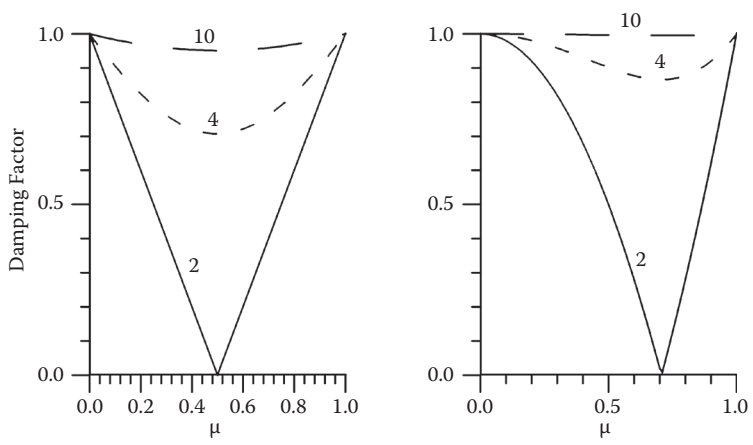


**FIGURE 9.2** Damping factor in the upstream scheme (left panel) and in the Lax–Wendroff scheme (right panel) for harmonic Fourier components. Labels give the wavelength of the components, nondimensionalized with the horizontal grid spacing.

becomes smaller. For  $\mu = 1$ , the solution is neutral, with  $|\lambda| = 1$  (the same is true for  $\mu = 0$ , but this corresponds to  $\Delta t = 0$ , which obviously is not an option for numerical time integration). In general, it may therefore be expected that after a sufficiently long time integration, small-scale features will have disappeared from the numerical solution. Figure 9.3 shows the calculated advection of two sine-waves (using numerical scheme (9.17)), as well as the analytical solution,

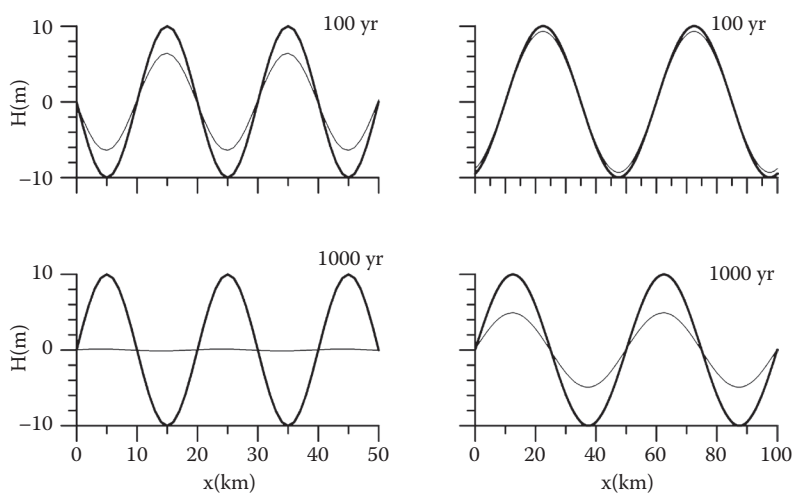


**FIGURE 9.3** Damping of two sine waves (left panels: wavelength equals 20 times the horizontal grid spacing; right panels: wavelength equals 50 times the horizontal grid spacing) for the upstream/forward-in-time approximation of the advection equation. The light curves represent the solution calculated numerically and the heavy curves the analytical solution.



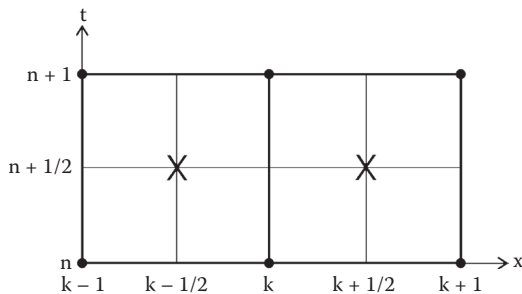


**FIGURE 9.4** Grid geometry for the Lax–Wendroff scheme.

obtained by simply moving the initial wave along the grid. As boundary conditions, the grid is assumed to be cyclic, with gridpoint  $x = -\Delta x$  corresponding to the last gridpoint,  $x = k_{\max} \cdot \Delta x$ . To minimize unwanted damping, the horizontal grid spacing,  $\Delta x$ , can be decreased. However, to satisfy the CFL condition for stability, the time step,  $\Delta t$ , must be decreased at the same time, and this may not always be practical.

A numerical scheme that performs better than (9.17) is the Lax–Wendroff scheme. The function  $H$  is known at the gridpoints  $k\Delta x$ , at time  $n\Delta t$ ; in Figure 9.4 these gridpoints are shown as black dots. Values of  $H$  at “intermediate” gridpoints (indicated by an  $X$  in Figure 9.4) are introduced to discretise the advection equation using central differencing for the  $x$ -derivative and the forward scheme for the time integration:

$$\frac{H_{k+1/2}^{n+1/2} - \frac{1}{2}(H_{k+1}^n + H_k^n)}{\frac{1}{2}\Delta t} = -U \frac{H_{k+1}^n - H_k^n}{\Delta x}. \quad (9.20)$$

Similarly

$$\frac{H_{k-1/2}^{n+1/2} - \frac{1}{2}(H_k^n + H_{k-1}^n)}{\frac{1}{2}\Delta t} = -U \frac{H_k^n - H_{k-1}^n}{\Delta x}. \quad (9.21)$$

The next step is to use central differencing, centered around  $(n + 1/2)\Delta t$ , to approximate the time derivative

$$\frac{H_k^{n+1} - H_k^n}{\Delta t} = -U \frac{H_{k+1/2}^{n+1/2} - H_{k-1/2}^{n+1/2}}{\Delta x}. \quad (9.22)$$

Using equations (9.20) and (9.21), the “intermediate” values on the right-hand side of (9.22) can be eliminated. The result is

$$\frac{H_k^{n+1} - H_k^n}{\Delta t} = -U \frac{H_{k+1}^n - H_{k-1}^n}{2\Delta x} + \frac{1}{2}U^2 \Delta t \frac{H_{k+1}^n - 2H_k^n + H_{k-1}^n}{(\Delta t)^2}, \quad (9.23)$$

or

$$H_k^{n+1} = \frac{1}{2}\mu(1+\mu)H_{k-1}^n + (1-\mu^2)H_k^n - \frac{1}{2}\mu(1-\mu)H_{k+1}^n, \quad (9.24)$$

with  $\mu = U \Delta t / \Delta x$ . Following the same procedure as above, it can be shown that this scheme is stable for  $\mu \leq 1$ , which is, once again, the CFL condition. The amplification factor is

$$|\lambda|^2 = 1 - 4\mu^2(1-\mu^2)\sin^4\left(\frac{\omega \Delta x}{2}\right). \quad (9.25)$$

Comparing this expression with the damping factor for the previously discussed numerical scheme (9.17) shows that damping is somewhat less of a problem in the Lax–Wendroff scheme (Figure 9.2, right panel). Applying the Lax–Wendroff scheme to the advection of sine-waves, as done in Figure 9.3 for the upstream/forward-in-time scheme, shows no significant difference between the numerically determined solution and the analytical solution.

The numerical schemes discussed above are examples of explicit schemes, in which the new value of  $H$  at a particular gridpoint is calculated independently of the other gridpoints. Such schemes have the great advantage of being fairly simple to construct, and solving them is straightforward. Their biggest disadvantage, however, is that the time step must be small to satisfy the CFL condition. This restriction can be avoided by using an implicit scheme. Such schemes are more complex to construct and solve than the explicit schemes discussed above, but may be more efficient because they are unconditionally stable and thus allow for a larger time step.

As an example of an implicit scheme, the Crank–Nicholson solution of the advection equation (9.6) is considered. Evaluating this equation at the intermediate time  $(n + 1/2) \cdot \Delta t$  gives

$$\begin{aligned} \left(\frac{\partial H}{\partial t}\right)_k^{n+1/2} &= -U \left(\frac{\partial H}{\partial x}\right)_k^{n+1/2} = \\ &= -U \left[ \left(\frac{\partial H}{\partial x}\right)_k^{n+1} + \left(\frac{\partial H}{\partial x}\right)_k^n \right]. \end{aligned} \quad (9.26)$$

The derivatives are now replaced by central differences, and all values of  $H$  at the new time  $(n + 1) \cdot \Delta t$  collected on the left-hand side. This gives

$$-\frac{1}{4}\mu H_{k-1}^{n+1} + H_k^{n+1} + \frac{1}{4}\mu H_{k+1}^{n+1} = \frac{1}{4}\mu H_{k-1}^n + H_k^n - \frac{1}{4}\mu H_{k+1}^n. \quad (9.27)$$

If  $k_{\max}$  represents the total number of gridpoints along the  $x$ -axis, equation (9.27) represents a set of  $k_{\max}$  linear equations that can be solved by matrix inversion. This is an expedient procedure because the coefficient-matrix is tridiagonal (that is, with nonzero elements only on the diagonal plus or minus one column). As a result, there is no need to formally invert the  $k_{\max}$  by  $k_{\max}$  coefficient-matrix (which contains

mostly zeros), and the solution can be coded very concisely (Press et al., 1992). When modeling glaciers, the advection velocity is not constant but depends nonlinearly on the ice thickness. This means that a fully implicit scheme becomes rather unpractical, as it requires the solution of a set of nonlinear equations.

The short introduction presented above highlights some of the more common problems encountered when constructing numerical models to simulate the behavior of ice sheets. The advection equation was chosen as example because this type of equation (hyperbolic equation) requires more stringent numerical schemes than do other types of equations. In particular, the diffusion equation is an example of a parabolic equation for which stable schemes are readily constructed that do not possess the nasty qualities discussed above (or, if they do, the effects are less manifest). For this reason, the continuity equation derived in Section 5.2 (which is an advection equation) is often recast as a diffusion equation. This is possible because the deformation of ice depends on the *gradient* of the quantity to be determined, namely, ice thickness, or rather, surface elevation. The next section discusses this issue in more detail.

### 9.3 MODEL DRIVEN BY SHEAR STRESS ONLY

To illustrate the steps involved in constructing numerical ice-flow models, this section starts with discussing the simplest model, namely, isothermal one-dimensional lamellar flow in the  $x$ -direction. In that case, the rate factor in the flow law is taken constant, and expressions for the depth-integrated ice flux are substituted in the continuity equation to compute evolution of ice thickness.

Where drag at the glacier base provides the sole resistance to flow, the depth-averaged ice velocity can be calculated from the lamellar flow model and is given by (Section 4.2)

$$U = \frac{2AH}{n+2} \tau_{dx}^n + U_b, \quad (9.28)$$

where  $U_b$  represents the sliding velocity. In the following discussion, basal sliding is not included so as to simplify the equations and more clearly demonstrate the procedure involved. Provided that the sliding velocity can be related to basal drag or driving stress (for example, using equation (7.9), or (7.41) if deformation of subglacial till is important), basal sliding is readily incorporated into the numerical model discussed in this section.

Conservation of ice volume is expressed by the continuity equation (5.18)

$$\frac{\partial H}{\partial t} = - \frac{\partial(HU)}{\partial x} + M. \quad (9.29)$$

Substituting expression (9.28) for the ice velocity into this equation gives

$$\frac{\partial H}{\partial t} = - \frac{\partial}{\partial x} \left( \frac{2A}{n+2} H^2 \tau_{dx}^n \right) + M. \quad (9.30)$$

The driving stress can be calculated from the ice thickness,  $H$ , and slope of the ice surface,  $\partial h/\partial x$  (Section 3.2) as

$$\tau_{dx} = -\rho g H \frac{\partial h}{\partial x}. \quad (9.31)$$

The continuity equation now becomes

$$\frac{\partial H}{\partial t} = + \frac{\partial}{\partial x} \left( \frac{2A}{n+2} (\rho g)^n H^{n+2} \left| \frac{\partial h}{\partial x} \right|^{n-1} \frac{\partial h}{\partial x} \right) + M, \quad (9.32)$$

or

$$\frac{\partial H}{\partial t} = \frac{\partial}{\partial x} \left( D \frac{\partial h}{\partial x} \right) + M. \quad (9.33)$$

This is a parabolic differential equation that may be interpreted as a diffusion equation for the ice thickness,  $H$ . The diffusivity

$$D = \frac{2A}{n+2} (\rho g)^n H^{n+2} \left| \frac{\partial h}{\partial x} \right|^{n-1}, \quad (9.34)$$

increases strongly with ice thickness and surface slope, due to the nonlinear character of Glen's flow law.

To solve the continuity equation (9.33) on a numerical grid, the diffusivity is first calculated at the gridpoints. To avoid confusion between exponents and grid coordinates, the following notation is used

$$H_{p,q} = H(p \cdot \Delta x, q \cdot \Delta t), \quad (9.35)$$

where  $p$  and  $q$  represent integer numbers. Using central differencing, the diffusivity is

$$D_{p,q} = C H_{p,q}^{n+2} \left( \frac{|h_{p+1,q} - h_{p-1,q}|}{2\Delta x} \right)^{n-1}, \quad (9.36)$$

with

$$C = \frac{2A}{n+2} (\rho g)^n, \quad (9.37)$$

containing all constants. Note that  $C$  may vary along the flowline if the rate factor,  $A$ , is not constant.

The next step is to calculate the ice flux at intermediate gridpoints, using interpolated values for the diffusivity

$$F_{p+1/2,q} = \frac{1}{2}(D_{p,q} + D_{p+1,q}) \frac{h_{p+1,q} - h_{p,q}}{\Delta x}. \quad (9.38)$$

Note that  $F = -HU$  represents minus the ice flux.

Using the forward scheme for the time derivative in the continuity equation (9.33), the new ice thickness can now be calculated from

$$H_{p,q+1} = H_{p,q} + \frac{\Delta t}{\Delta x}(F_{p+1/2,q} - F_{p-1/2,q}) + M \Delta t. \quad (9.39)$$

The time step that can be used is rather small. For a linear diffusion equation (that is, an equation like (9.33) but with constant diffusivity,  $D$ ), the criterion for stability is (Smith, 1985)

$$\Delta t \leq \frac{(\Delta x)^2}{4D}. \quad (9.40)$$

In first approximation, this criterion may be used to estimate the maximum allowable time step for the nonlinear equation (9.39). A typical value for  $D$  is about  $10^7$  m<sup>2</sup>/yr but may be (much) larger near the edge of the ice sheet or at the start of an integration when the ice sheet is far from equilibrium. Taking a moderate grid spacing of 10 km, the maximum time step is only about 2.5 yr.

To numerically integrate the continuity equation, boundary conditions need to be imposed at the ends of the model domain. Strictly speaking, the starting profile (which may be zero ice thickness everywhere) is also a boundary condition, applying to  $t = 0$  yr. However, it is common usage to refer to this “boundary” condition as the initial condition. Which other boundary conditions are used depends on the particular ice sheet being modeled. Of course, one should be careful not to impose boundary conditions that are too restrictive, such as prescribing the ice thickness at both ends of the model domain, or the ice flux at one end and the ice thickness at the other end.

As an example, consider the simple geometry of a horizontal continent bounded on one side by a deep ocean. At this end, the ice thickness is set to zero because the ice sheet cannot advance into the deep ocean. The surface mass balance is prescribed as a function of distance only, and decreasing toward the south

$$M = 0.5 - 0.5 \cdot 10^{-6} x, \quad (9.41)$$

with  $M$  in m ice depth per year and  $x$  the distance (in m) from the northern edge.  $M$  becomes negative (representing ablation) at  $x = 1000$  km. Because the surface mass balance becomes sufficiently negative for a large distance, no boundary condition

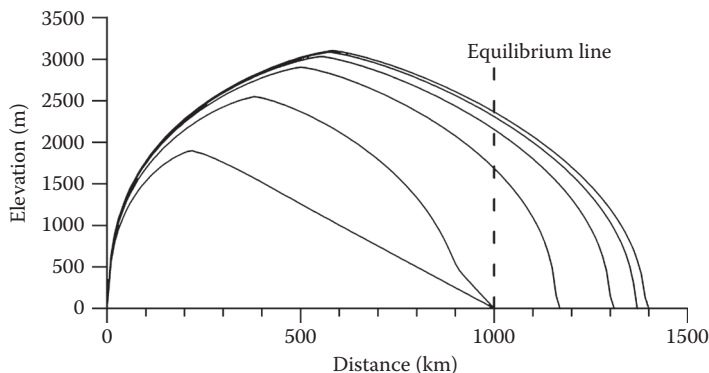


**FIGURE 9.5** Results from a numerical integration of an ice sheet on a horizontal bed, bounded to the north (at 0 km) by a polar ocean. Profiles are shown for 1, 5, 10, 20, 30, 40, and 50 kyr of simulated time. The surface mass balance decreases linearly toward the south (in the direction of the x-axis).

needs to be prescribed at the lower end, other than that the ice thickness cannot become negative. Figure 9.5 shows the results of an integration starting with zero ice thickness everywhere. The horizontal grid spacing,  $\Delta x$ , equals 10 km and the time step,  $\Delta t$ , one year. At first, snow accumulates in areas at or above sea level where the surface mass balance is positive. After the ice cover becomes sufficiently thick, the ice starts to flow toward both margins, and in particular into the region with surface ablation. The southern edge of the ice sheet jumps from one gridpoint to the next, but this does not affect the results in a serious way. Changing the grid spacing leads to virtually the same ice-sheet profile as that shown in Figure 9.5. Apparently, if the ice-sheet edge is located in a region with negative surface mass balance, the margin position is well-defined and determined by large-scale ice sheet dynamics and consideration of mass conservation, rather than by the small-scale mechanics of the glacier snout.

The reason that the glacier snout advances is that the ice flux just beyond the edge is not zero, but determined by the diffusivity at the last gridpoint covered with ice. Thus, at the next gridpoint, the diffusion term in the continuity equation is nonzero, and positive in general, allowing a small layer of ice to form. This scheme works well where the bed is above sea level, but another treatment of the movement of the glacier edge is needed where the bed slopes downward below sea level. If the position of the glacier edge is defined by the flotation criterion (that is,  $H$  is set to zero when the ice becomes too thin to rest on the seafloor), the edge cannot advance. Using the continuity equation (9.33) to calculate the thickness change at the first gridpoint beyond the edge, the new ice thickness is a few meters at most, depending on the time step. In general, this is too small to overcome the flotation criterion where the bed is more than a few meters below sea level, and the thickness is set to zero. To allow for expansion of an ice sheet into a (shallow) sea, the formation of an ice shelf needs to be considered.

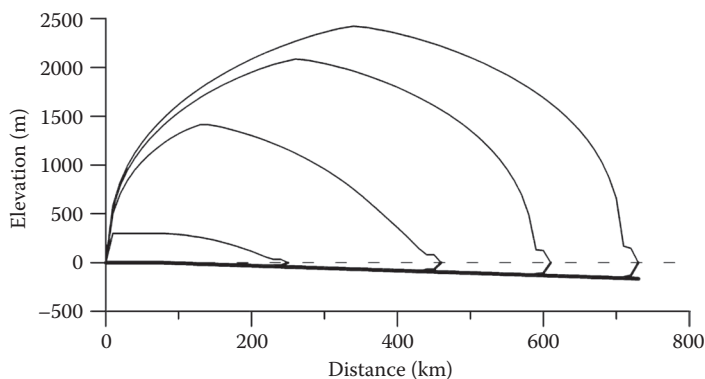


**FIGURE 9.6** Results from a numerical integration of an ice sheet on a bed with constant slope, bounded to the north (at 0 km) by a polar ocean. Profiles are shown for 1, 5, 10, and 20 kyr of simulated time. The surface mass balance is taken constant.

The flow of ice shelves is governed by a balance between driving stress and resistance from gradients in longitudinal stress and lateral drag. As a result, modeling ice-shelf flow is essentially different from modeling lamellar flow, in which the driving stress is balanced entirely by drag at the glacier bed. It is possible to couple the two flow regimes to obtain a complete model for a grounded ice sheet discharging into an ice shelf to study the migration of the grounding line in more detail as discussed in Section 9.4. However, as a start, a simpler procedure can be adopted. Ice shelves react rather quickly to changes in environmental conditions (Van der Veen, 1986) and, in approximation, may be taken to be in equilibrium with their environment. In that case, the ice-shelf profile can be calculated using the equilibrium profiles derived in Section 5.5. Migration of the ice-sheet edge becomes possible if the ice shelf becomes sufficiently thick to run aground.

Figure 9.6 shows the growth of an ice sheet on a sloping bed. At the northern edge, the bed is just above sea level over a distance of 70 km, in order to initiate ice-sheet growth. The surface accumulation rate is constant, equal to 0.3 m/yr. The grounding line is assumed to be at the last gridpoint with grounded ice, and the thickness and speed at this point are used in the calculation of the ice-shelf profile (equation (5.77) for positive surface mass balance). As the grounded portion of the ice sheet builds up, the ice shelf also becomes thicker, until its thickness exceeds the flotation thickness and the ice-sheet edge advances one gridpoint.

It is important to test numerical models, whenever possible, against available data or against analytical solutions. Figure 9.7 shows the profile of an ice sheet on a horizontal bed with constant surface accumulation as calculated with the numerical model and according to the Vialov-profile (5.39). In the numerical model, the upstream boundary condition is  $H(1) = H(2)$ , so the ice divide is halfway in between the first two gridpoints. Prescribing the half-width at 505 km, the edge of the ice sheet is at  $x = 510$  km. As the figure shows, the computed and analytical profiles are

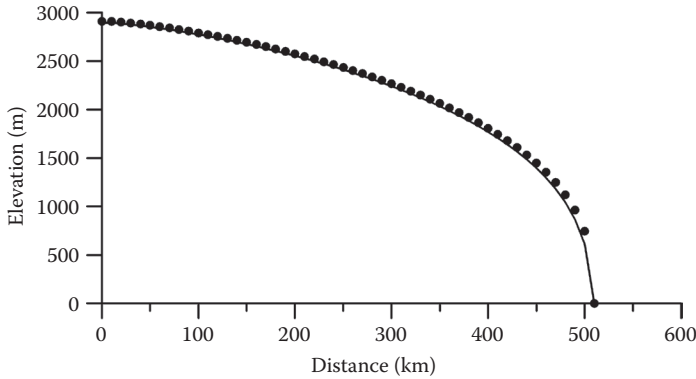


**FIGURE 9.7** Comparison between the steady state ice-sheet profile calculated with the numerical model, and the analytical equilibrium profile (represented by the dots).

virtually the same. Of course, this is not a validation of the model per se. Rather, it shows that the numerical integration scheme is consistent with the analytical solution of the equations that the model tries to solve. Whether or not these equations actually apply depends on the particular situation being modeled. Time-dependent analytical solutions against which the model can be compared are discussed in Section 10.3.

The numerical model described above is readily expanded to include both horizontal directions. In that case, the diffusivity becomes

$$D = CH^{n+2} \left( \left( \frac{\partial h}{\partial x} \right)^2 + \left( \frac{\partial h}{\partial y} \right)^2 \right)^{(n-1)/2}, \quad (9.42)$$

and the continuity equation is

$$\frac{\partial H}{\partial t} = + \frac{\partial}{\partial x} \left( D \frac{\partial h}{\partial x} \right) + \frac{\partial}{\partial y} \left( D \frac{\partial h}{\partial y} \right) + M. \quad (9.43)$$

These equations can be solved similarly as for the one-dimensional case (equation (9.39)), but to keep the solution stable, a relatively coarse horizontal grid has to be used (for example, Oerlemans, 1982). To allow for a finer grid size, most models employ somewhat different and more efficient solution schemes. For example, the Glimmer community ice sheet model includes three methods for solving this equation on a discrete numerical grid, namely, the alternating direction implicit method, a linearized semi-implicit method, and a nonlinear scheme (Rutt et al., 2009). These three methods are briefly described below.

To improve numerical stability, two staggered horizontal grids are used, with the same grid spacings,  $\Delta x$  and  $\Delta y$ , and offset by half a grid spacing (Figure 9.8). Following the notation of Rutt and others (2009), the grids are referred to as the (i, j) grid and the (r, s) grid. Ice thickness and ice flux are calculated on the (i, j) grid,



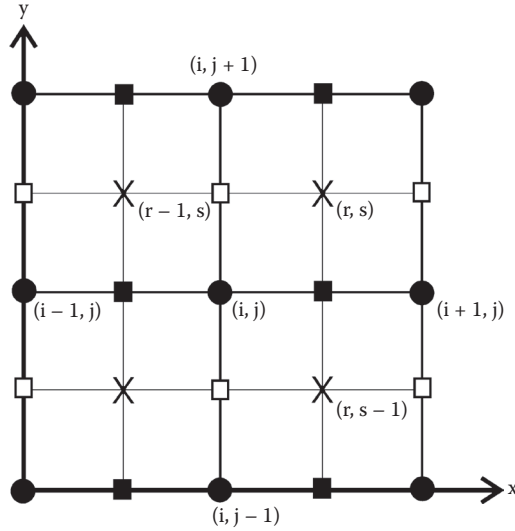


**FIGURE 9.8** Grid geometry used in the Glimmer community ice sheet model. Ice thickness is known on the  $(i, j)$  grid (filled circles); the ice flux is calculated on the  $(i, j)$  grid at intermediate points: filled squares indicate where the flux in the  $x$ -direction is calculated, and open squares indicate where the flux in the  $y$ -direction is calculated. Diffusivities are calculated on the  $(r, s)$  grid, indicated by the  $X$ .

while diffusivities are calculated on the  $(r, s)$  grid. The diffusivity is proportional to the surface slope in both directions and these are estimated as

$$\left( \frac{\partial h}{\partial x} \right)_{r,s} = \frac{h_{i+1,j} - h_{i,j} + h_{i+1,j+1} - h_{i,j+1}}{2 \Delta x}, \quad (9.44)$$

$$\left( \frac{\partial h}{\partial y} \right)_{r,s} = \frac{h_{i,j+1} - h_{i,j} + h_{i+1,j+1} - h_{i+1,j}}{2 \Delta y}. \quad (9.45)$$

Ice thickness at gridpoint  $(r, s)$  is obtained by averaging values at the four surrounding gridpoints

$$H_{r,s} = \frac{1}{4} (H_{i,j} + H_{i+1,j} + H_{i+1,j+1} + H_{i,j+1}). \quad (9.46)$$

The ice flux in the  $x$ -direction is calculated at halfway points in the  $(i, j)$  grid (Figure 9.8; compare with equation (9.38)) as

$$F_{i+1/2,j}^x = \frac{1}{2} (D_{r,s} + D_{r,s-1}) \frac{h_{i+1,j} - h_{i,j}}{\Delta x}. \quad (9.47)$$

Similarly, the ice flux in the other horizontal direction is

$$F_{i,j+1/2}^y = \frac{1}{2}(D_{r,s} + D_{r-1,s}) \frac{h_{i,j+1} - h_{i,j}}{\Delta x}. \quad (9.48)$$

The first approach to discretize the continuity equation is the alternating direction implicit (or ADI) method, based on the Peaceman–Rachford formula (Mitchell and Griffiths, 1980, p. 59; c.f. Press et al., 1992, p. 861 ff). Although this scheme is not unconditionally stable because of the nonlinear dependence of the ice speed on the surface slope, it allows time steps that are an order of magnitude larger than can be used in the explicit approach, without a noticeable loss of accuracy (Huybrechts, 1992). The ADI method involves a two-step procedure. First, the ice thickness is calculated at the intermediate time,  $t + 1/2 \Delta t$ , using an implicit scheme for the  $x$ -derivatives and the old values for the  $y$ -derivatives. Thus, the continuity equation is discretized as

$$2 \frac{H_{i,j}^{t+1/2} - H_{i,j}^t}{\Delta t} = \frac{F_{i+1/2,j}^{x,t+1/2} - F_{i-1/2,j}^{x,t+1/2}}{\Delta x} + \frac{F_{i,j+1/2}^{y,t} - F_{i,j-1/2}^{y,t}}{\Delta y} + M_{i,j}. \quad (9.49)$$

Collecting all terms involving  $t + 1/2$  on the left-hand side gives a set of tridiagonal equations for each grid row ( $y = \text{constant}$ ) that can be solved for each row separately. Next, the implicit direction is reversed: the intermediate values are used to estimate the  $x$ -derivatives, while the  $y$ -derivatives are approximated by an implicit scheme. That is, the continuity equation is approximated as

$$2 \frac{H_{i,j}^{t+1} - H_{i,j}^{t+1/2}}{\Delta t} = \frac{F_{i+1/2,j}^{x,t+1/2} - F_{i-1/2,j}^{x,t+1/2}}{\Delta x} + \frac{F_{i,j+1/2}^{y,t+1} - F_{i,j-1/2}^{y,t+1}}{\Delta y} + M_{i,j}. \quad (9.50)$$

Again, the resulting set of equations is solved for each grid column ( $x = \text{constant}$ ) separately. A fuller description of this method can be found in Huybrechts (1992) or Rutt and others (2009).

The second numerical solution scheme implemented in the Glimmer model is a linearized semi-implicit method using the Crank–Nicholson scheme. Analogous to equation (9.26), the continuity equation is discretized as

$$\begin{aligned} \frac{H_{i,j}^{t+1} - H_{i,j}^t}{\Delta t} = & \frac{F_{i+1/2,j}^{x,t+1} - F_{i-1/2,j}^{x,t+1}}{2 \Delta x} + \frac{F_{i,j+1/2}^{y,t+1} - F_{i,j-1/2}^{y,t+1}}{2 \Delta y} \\ & + \frac{F_{i+1/2,j}^{x,t} - F_{i-1/2,j}^{x,t}}{2 \Delta x} + \frac{F_{i,j+1/2}^{y,t} - F_{i,j-1/2}^{y,t}}{2 \Delta y} + M_{i,j}. \end{aligned} \quad (9.51)$$

The ice flux at time  $t + 1$  is calculated using diffusivities from the current time step and surface elevations at  $t + 1$ . That is

$$F_{i+1/2,j}^{x,t+1} = \frac{1}{2}(D_{r,s}^t + D_{r,s}^{t+1}) \frac{h_{i+1,j}^{t+1} - h_{i,j}^{t+1}}{\Delta x}. \quad (9.52)$$

Equation (9.51) can be rearranged by collecting all the terms that involve thickness and surface elevation at time  $t + 1$  on the left-hand side and moving the remaining terms to the right-hand side. This yields a set of  $i_{\max} \times j_{\max}$  equations that can be solved using an iterative matrix solver. The lengthy equations can be found in Rutt and others (2009).

The third scheme to solve the continuity equation involves Picard iteration. In essence, the discrete continuity equation (9.51) is solved multiple times with diffusivities recalculated at each iteration step using the geometry from the previous iteration. This procedure is repeated until for all gridpoints the difference in ice thickness between successive iterations is smaller than some prescribed threshold value (Rutt et al., 2009).

## 9.4 FLOWBAND MODEL

The flowline model discussed in Section 9.3 is based on the assumption that the driving stress is balanced by drag at the glacier base (lamellar flow). This is not a realistic model for marine terminating outlet glaciers where gradients in longitudinal stress and lateral drag may be important in the balance of forces. Several full-stress flowband models have been developed, but these are based on the assumption of plane flow and do not incorporate lateral drag (for example, Hindmarsh, 2004; Price et al., 2007; Aschwanden and Blatter, 2009). Van der Veen and Whillans (1996) describe a model for an active ice stream with resistance to flow partitioned between basal and lateral drags. That model was extended to include gradients in longitudinal stress by Nick et al. (2009, 2010, 2012) and is described in this section.

The continuity equation (5.18) expresses conservation of ice volume along a flowband of constant width. To allow for diverging or converging flow, the width along the flowband is allowed to vary. Denoting the cross-sectional area by  $S$ , the continuity equation becomes

$$\frac{\partial S}{\partial t} = - \frac{\partial F}{\partial x} + 2 M W, \quad (9.53)$$

where  $F$  represents the ice flux through the cross-section and  $W$  the half-width measured at the glacier surface. Neglecting effects from sloping side walls, the ice flux is given by  $F = 2 H U W$ , with  $U$  the depth-averaged horizontal ice velocity averaged over the width of the glacier. Van der Veen and Whillans (1996) allow the width to change over time as the ice stream margins migrate inward or outward, but here the width is considered fixed in time. The continuity equation is then

$$\frac{\partial H}{\partial t} = - \frac{1}{2W} \frac{\partial F}{\partial x} + M. \quad (9.54)$$

The next step is to derive an equation from which the velocity,  $U$ , can be estimated. This requires consideration of force balance.

Force balance is expressed by equation (3.22). Most outlet glaciers are moving rapidly as a result of basal sliding, and the resistive stresses,  $R_{xx}$  and  $R_{yy}$ , may be considered constant with depth, and the balance equation becomes

$$\tau_{dx} = \tau_{bx} - \frac{\partial}{\partial x}(HR_{xx}) - \frac{\partial}{\partial y}(HR_{xy}). \quad (9.55)$$

The driving stress is calculated from the geometry of the glacier as

$$\tau_{dx} = -\rho g H \frac{\partial h}{\partial x}, \quad (9.56)$$

where  $\rho$  represents the ice density and  $h$  the surface elevation, taken to be constant in the transverse direction. The resistive stresses on the right-hand side of equation (9.55) can each be written in terms of the horizontal velocity,  $U$ .

The contribution from internal deformation to ice flow is ignored and all flow assumed to be associated with basal sliding. Adopting the modified Weertman sliding relation, basal drag is related to the sliding velocity as equation (7.25)

$$\tau_{bx} = \mu B_s N^q U^p, \quad (9.57)$$

where  $B_s$  is a sliding constant and  $\mu$  a bed friction parameter that may be related to bed roughness and amount of basal water. Following Nick et al. (2010), the effective pressure at the bed,  $N$ , is set equal to the height above buoyancy (equation (7.57)), implying an easy connection between the subglacial drainage system and the open ocean. The sliding relation (9.57) then becomes

$$\tau_{bx} = \mu B_s \left( H - \frac{\rho_w}{\rho} D \right)^q U^p, \quad (9.58)$$

with  $\rho_w$  the density of water, and  $D$  the depth of the bed below sea level.

The stretching stress,  $R_{xx}$ , is linked to the stretching rate,  $\dot{\epsilon}_{xx}$ , through the flow law (3.48). Neglecting the contribution of strain rates other than the stretching rate to the effective strain rate, the longitudinal stress is

$$R_{xx} = 2B \dot{\epsilon}_{xx}^{1/n} = 2B \left( \frac{\partial U}{\partial x} \right)^{1/n}, \quad (9.59)$$

and

$$\frac{\partial}{\partial x}(HR_{xx}) = 2B \frac{\partial}{\partial x} \left[ H \left( \frac{\partial U}{\partial x} \right)^{1/n} \right]. \quad (9.60)$$

The viscosity parameter,  $B$ , is taken constant along the flowline. Following the model described in Section 4.4, the assumption is made that resistance to flow from

lateral drag is equally important across the full width of the glacier, and the lateral shear stress,  $R_{xy}$ , varies linearly across the glacier. Resistance to flow associated with lateral drag is then

$$F_s = \frac{H\tau_s}{W}, \quad (9.61)$$

where  $\tau_s$  represents the shear stress at the lateral margins. The corresponding transverse velocity profile is

$$U(y) = \left[ 1 - \left( \frac{y}{W} \right)^{n+1} \right] \frac{2W}{n+1} \left( \frac{\tau_s}{B} \right)^n, \quad (9.62)$$

with  $y = 0$  at the center line. Averaging this expression over the width of the glacier gives

$$U = \frac{2W}{n+2} \left( \frac{\tau_s}{B} \right)^n. \quad (9.63)$$

Resistance to flow from lateral drag can now be written as

$$F_s = \frac{BH}{W} \left( \frac{(n+2)U}{2W} \right)^{1/n}. \quad (9.64)$$

Force balance can now be expressed in terms of the velocity,  $U$ , and its along-flow gradient,  $\partial U/\partial x$ . Substituting equations (9.56), (9.58), (9.60), and (9.64) in the balance equation (9.55) yields

$$-\rho g H \frac{\partial h}{\partial x} = \mu B_s \left( H - \frac{\rho_w}{\rho} D \right)^q U^p - 2B \frac{\partial}{\partial x} \left[ H \left( \frac{\partial U}{\partial x} \right)^{1/n} \right] + \frac{BH}{W} \left( \frac{(n+2)U}{2W} \right)^{1/n}. \quad (9.65)$$

Inspection of this equation shows that at each location the velocity depends not only on the local geometry but also on neighboring velocities through the term involving gradients in longitudinal stress (the second term on the right-hand side). This means that the continuity equation cannot be written as a diffusion equation, and each time step the velocity has to be found by numerical iteration.

Nick et al. (2010) solve the force-balance equation (9.65) using the Newton iteration method (Press et al., 1992, Section 9.4). This method, also referred to as the method of tangents, is illustrated in [Figure 9.9](#) and consists of extending the tangent line until it crosses zero to find the next guess. The balance equation is formally written as  $G(U) = 0$ , with derivative  $G'(U) = \partial G(U)/\partial U$ . Denoting successive guesses for the velocity by the subscript  $k$ , this iteration scheme is

$$U_k = U_{k-1} - \frac{G(U_{k-1})}{G'(U_{k-1})}. \quad (9.66)$$

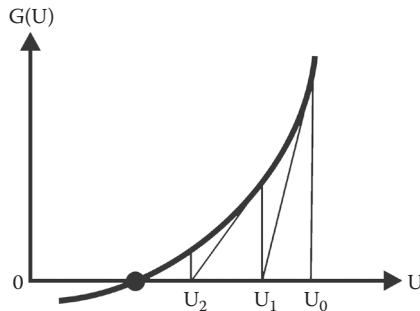


**FIGURE 9.9** Illustrating the Newton iteration method.

The correct solution is reached when  $G(U)$  is sufficiently small at all gridpoints. The iteration is somewhat complicated because the balance function,  $G(U)$ , depends not only on the velocity at the gridpoint under consideration but also on the values at the two neighboring gridpoints. Convergence usually occurs within a few iteration steps.

The numerical model employs a variable grid with the first gridpoint fixed at the upstream boundary, taken to be the ice divide. Ice thickness is evaluated at gridpoints, while velocity and the ice flux are calculated at intermediate gridpoints to keep the solution scheme stable. The last gridpoint is at the calving terminus, and the grid spacing is adjusted each time step as the terminus advances or retreats. Because of the high spatial resolution (a few hundred meters), grounding-line motion was found to be independent of the grid spacing. In the case where a floating ice tongue forms, a smooth transition in basal resistance from the grounded ice to the floating part is achieved because basal drag is inversely proportional to the effective basal pressure; this term decreases to near zero toward the grounding line as the glacier thins and approaches flotation.

Two boundary conditions are required for the numerical model. The upglacier boundary corresponds to the ice divide, and the surface slope and ice velocity are set to zero. The boundary condition at the calving terminus follows from the requirement that averaged over the ice thickness, the full stress,  $\sigma_{xx}(z) = R_{xx} - \rho g(h - z)$ , must be zero. The depth-averaged full stress is

$$\bar{\sigma}_{xx} = \frac{1}{H} \int_{-D}^h \sigma_{xx}(z) dz = R_{xx} - \frac{1}{2} \rho g H. \quad (9.67)$$

This stress is partly balanced by water pressure where the bed is below sea level. Averaged over the ice thickness, the water pressure is

$$\bar{\sigma}_w = \frac{1}{H} \int_{-D}^0 \rho_w g z dz = -\frac{1}{2} \rho_w g \frac{D^2}{H}. \quad (9.68)$$

From these two expressions, and setting  $\bar{\sigma}_{xx}$  equal to zero, the resistive stretching stress at the terminus is found to be given by

$$R_{xx}(L) = \frac{1}{2} \rho g \left( H - \frac{\rho_w}{\rho} \frac{D^2}{H} \right). \quad (9.69)$$

For a floating terminus, this expression is equivalent to the solution derived in Section 4.5 for a free-floating ice shelf spreading in the along-flow direction only. Sea ice, or a mélange of icebergs and bergy bits present in the proglacial fjord, may exert a (small) back stress,  $\sigma_b$ , on the calving terminus (Amundson et al., 2010), which would lower  $R_{xx}(L)$ . Including this back stress, the stretching rate at the terminus is

$$\frac{\partial U}{\partial x} = A \left[ \frac{\rho g}{4} \left( H - \frac{\rho_w}{\rho} \frac{D^2}{H} - \frac{\sigma_b}{\rho g} \right) \right]^n. \quad (9.70)$$

In addition to the two velocity boundary conditions at both ends of the model domain, a calving criterion is needed to constrain the position of the calving front. Any of the calving relations discussed in Section 8.5 can be implemented. For the water-depth model, in which calving rate is proportional to the water depth at the terminus, at each time step the new terminus position is determined by the difference between the forward ice velocity and the calving rate causing the terminus to retreat. For the height-above-buoyancy calving model, the terminus position is at the location where the local ice thickness equals the minimum thickness required for the terminus to maintain the specified height above buoyancy. Similarly, for the crevasse-depth models, the position of the terminus is determined by the location where surface crevasses penetrate to sea level or where surface and bottom crevasses penetrate the full ice thickness.

The primary value of the flowband model is its ability to investigate how different external forcings may affect flow and stability of calving glaciers. All physical processes are included in a more or less realistic way: basal sliding, lateral drag, gradients in longitudinal stress, and iceberg calving. Internal deformation and proglacial sedimentation can be readily included if needed (Nick et al., 2009). Vieli and Nick (2011) and Nick et al. (2012) discuss series of model experiments aimed at identifying processes that may lead to large changes on Greenland outlet glaciers. Some of the results obtained with this flow-band model are discussed in Section 8.5.

## 9.5 CALCULATING THE TEMPERATURE FIELD

As discussed in Section 2.2, the rate of deformation of glacier ice depends strongly on the ice temperature, and glacier flow should be treated as a thermomechanically coupled problem. This means that the velocity and temperature must be determined simultaneously. The first attempt to do this is described by Jenssen (1977), who used a three-dimensional model to numerically solve the continuity and thermodynamic

equations. Applying the numerical scheme to the Greenland Ice Sheet led to numerical instabilities, however, forcing time integrations to be discontinued after 1000 years of simulated evolution. To a large extent, this shortcoming may be attributed to the coarse grid used by Jenssen (1977). Available computer capacity restricted the size of the grid to 12 gridpoints in the east–west direction (spacing of 100 km), 12 gridpoints in the north–south direction (spacing of 200 km), and 10 gridpoints in the vertical (spacing varying from 5 to 300 m). In spite of the obvious disappointing performance of his model, the attempt by Jenssen (1977) can be considered the first successful model in which the ice flow is coupled to the temperature in a truly dynamic fashion. Later models are essentially the same as the Jenssen model, but more successful because of increased computer resources (allowing a finer grid) and perhaps more sophisticated numerical techniques than those used by Jenssen (1977).

The thermomechanical model consists of two parts, namely, solving the continuity equation for the evolution of the ice-sheet geometry, and solving the thermodynamic equation to obtain the ice temperature needed to calculate the rate factor in the continuity equation. In the most elaborate models (Jenssen, 1977; Huybrechts and Oerlemans, 1988; Rutt et al., 2009), the temperature is calculated on a two- or three-dimensional grid covering one or two horizontal directions and the vertical. Here, the two-dimensional ( $x, z$ ) model is discussed to illustrate the principles. Because the ice-sheet geometry varies along the flowline, it is convenient to use the dimensionless vertical coordinate,  $s$ , introduced in Section 4.1, with  $s = 0$  at the ice surface and  $s = 1$  at the bed.

Conservation of heat is expressed by the thermodynamic equation (6.17). Horizontal diffusion of heat is assumed to be small compared with vertical diffusion, and internal melting (the last line in equation (6.17)) is neglected. Finally, lamellar flow is considered, with vertical shearing the only strain rate contributing to strain heating. The temperature equation then reduces to

$$\frac{\partial T}{\partial t} = -u \frac{\partial T}{\partial x} - w \frac{\partial T}{\partial z} + K \frac{\partial^2 T}{\partial z^2} + \frac{2}{\rho C_p} \dot{\epsilon}_{xz} \tau_{xz}. \quad (9.71)$$

This equation is valid in the ( $x, z$ ) coordinate system. To obtain its equivalent for the ( $x, s$ ) coordinate system, the transformation formulas derived in Section 4.1 are used to write derivatives in the ( $x, z$ ) system in terms of ( $x, s$ ) derivatives. However, the model domain may change as the ice sheet evolves, which means that at a certain gridpoint, the level  $s$  does not always correspond to the same physical depth. In other words, the temperature  $T(s)$  may change as the ice thickness changes, even if the glacier was otherwise in thermal equilibrium. To account for this, the time derivative also needs to be rewritten. Similar to the derivation leading to equation (4.6), the following correspondence is found

$$\left( \frac{\partial T}{\partial t} \right)_z = \left( \frac{\partial T}{\partial t} \right)_s + \frac{1}{H} \left( \frac{\partial h}{\partial t} - s \frac{\partial H}{\partial t} \right) \left( \frac{\partial T}{\partial s} \right)_x. \quad (9.72)$$



Rewriting all derivatives, equation (9.71) becomes, in the  $(x, s)$  coordinate system

$$\begin{aligned} \left( \frac{\partial T}{\partial t} \right)_s = & -\frac{1}{H} \left( \frac{\partial h}{\partial t} - s \frac{\partial H}{\partial t} \right) \left( \frac{\partial T}{\partial s} \right)_x - u(s) \left( \frac{\partial T}{\partial x} \right)_s - \frac{u(s)}{H} \left( \frac{\partial h}{\partial x} - s \frac{\partial H}{\partial x} \right) + \\ & + \frac{w(s)}{H} \left( \frac{\partial T}{\partial s} \right)_x + \frac{K}{H^2} \left( \frac{\partial^2 T}{\partial s^2} \right)_x + \frac{2}{\rho C_p} \dot{\epsilon}_{xz} \tau_{xz}. \end{aligned} \quad (9.73)$$

The next step is to calculate the velocity field and the strain heating at depth. For lamellar flow, the driving stress is balanced by drag at the glacier base, and the vertical shear strain rate becomes (c.f. Section 4.2)

$$\dot{\epsilon}_{xz} = A s \tau_{dx}^3, \quad (9.74)$$

using  $n = 3$  for the exponent in the flow law. Integrating from the base ( $s = 1$ ) to some level  $s$  in the ice gives the velocity at that level

$$u(s) = U_b + 2H\tau_{dx}^3 \int_s^1 A \bar{s}^3 d\bar{s}, \quad (9.75)$$

where  $U_b = u(1)$  represents the sliding velocity. The vertical velocity follows from the incompressibility condition (1.39). In the  $(x, s)$  system, this gives

$$\left( \frac{\partial w}{\partial s} \right)_x = H \left( \frac{\partial u}{\partial x} \right)_s + \left( \frac{\partial h}{\partial x} - s \frac{\partial H}{\partial x} \right) \left( \frac{\partial u}{\partial s} \right)_x. \quad (9.76)$$

At the surface, the vertical velocity is (taken positive when upward)

$$w(0) = \frac{\partial h}{\partial t} + u(0) \frac{\partial h}{\partial x} - M. \quad (9.77)$$

Integrating equation (9.76) from the surface to some depth  $s$  gives the vertical velocity

$$w(s) = \frac{\partial h}{\partial t} + u(s) \left( \frac{\partial h}{\partial x} - s \frac{\partial H}{\partial x} \right) + \int_0^s \left( H \frac{\partial u}{\partial x} + u \frac{\partial H}{\partial x} \right) d\bar{s}. \quad (9.78)$$

Finally, strain heating at level  $s$  is

$$Q(s) = \frac{2\tau_{dx}^4}{\rho C_p} A s^4. \quad (9.79)$$

With these expressions, the change in temperature can be calculated. The horizontal velocity is determined first, using the old temperatures to calculate the rate factor at depth. Next, the vertical velocity and strain heating are calculated. Substitution into the thermodynamic equation (9.73) gives  $\partial T/\partial t$ , allowing the new temperature to be estimated for time  $t + \Delta t$ .

The most efficient numerical scheme for solving the thermodynamic equation is a semi-implicit scheme. To illustrate how such a scheme is constructed, equation (9.73) is written as

$$\frac{\partial T}{\partial t} = a \frac{\partial^2 T}{\partial s^2} + b \frac{\partial T}{\partial s} + c \frac{\partial T}{\partial x} + d, \quad (9.80)$$

in which the coefficients,  $a$ ,  $b$ ,  $c$ , and  $d$ , are depth dependent and calculated using the old temperature. The horizontal advection term is also estimated from the old temperatures. The finite difference form of equation (9.80) is obtained analogous to the Crank–Nicholson approximation (9.27) discussed in Section 9.2. The result is

$$\begin{aligned} & \left( -\frac{a}{2(ds)^2} + \frac{b}{4ds} \right) T_{p,r-1,q+1} + \left( \frac{1}{\Delta t} + \frac{a}{(ds)^2} \right) T_{p,r,q+1} + \\ & + \left( -\frac{a}{2(ds)^2} - \frac{b}{4ds} \right) T_{p,r+1,q+1} = \\ & = \left( -\frac{a}{2(ds)^2} - \frac{b}{4ds} \right) T_{p,r-1,q} + \left( \frac{1}{\Delta t} - \frac{a}{(ds)^2} \right) T_{p,r,q} + \\ & + \left( \frac{a}{2(ds)^2} + \frac{b}{4ds} \right) T_{p,r+1,q} + \frac{c}{\Delta x} (T_{p,r,q} - T_{p-1,r,q}) + d. \end{aligned} \quad (9.81)$$

In this expression, the subscripts  $p$  and  $r$  refer to the horizontal and vertical directions, respectively, and the subscript  $q$  to the time steps. Note that the horizontal advection term is approximated by upstream differencing to improve stability. At every horizontal gridpoint,  $p \cdot \Delta x$ , this set of tridiagonal equations is solved for the new temperatures at depth levels  $r \cdot ds$  to obtain the new temperature at time  $(q + 1) \cdot \Delta t$ . The boundary conditions are the surface temperature,

$$T(0) = T_{\text{air}} - \gamma_a h, \quad (9.82)$$

where  $T_{\text{air}}$  represents the air temperature at sea level and  $\gamma_a$  the atmospheric lapse rate, and the temperature gradient at the glacier base,

$$\left( \frac{\partial T}{\partial s} \right)_{s=1} = + \frac{\gamma_g}{H} + \frac{\tau_{dx} U_b}{kH}. \quad (9.83)$$

In this last expression,  $\gamma_g$  represents the geothermal heat flux and  $k$  the thermal conductivity of ice. The first term on the right-hand side of equation (9.83) represents inflow of geothermal heat and the second term generation of heat at the glacier bed by basal sliding. Note that while the temperature near the base should decrease from the bed upward, the temperature gradient  $\partial T/\partial s(1)$  is positive because the dimensionless vertical coordinate,  $s$ , increases toward the bed.

The evolution of the ice sheet is described by the continuity equation. The solution scheme is similar to that described in the previous section. The only difference is that the depth-averaged rate factor used in equation (9.34) for the diffusivity needs to be replaced by the vertical-mean value based on the calculated temperatures. This leads to the following expression for the diffusivity:

$$D = 2(\rho g)^3 H^5 \left| \frac{\partial h}{\partial x} \right|^2 \int_0^1 \int_s^1 A \bar{s}^3 d\bar{s}. \quad (9.84)$$

The Glimmer community ice-sheet model uses an iterative scheme to solve the temperature equation. For each column under consideration, the horizontal advection terms are estimated using temperatures at adjacent columns from the previous iteration. The remaining unknown temperatures in the column are discretized using the time-implicit Crank–Nicholson method to form a tridiagonal matrix equation. This scheme usually converges within a few iteration steps (Rutt et al., 2009).

## 9.6 GEODYNAMICS

The weight of ice sheets exerts a pressure on the underlying bedrock, which in response will deflect downward to restore equilibrium of forces. The deflection can be considerable under the central parts of ice sheets. For example, the Antarctic Ice Sheet is in places more than 4500 m thick. The equilibrium adjustment of the bed is roughly one-third of the ice thickness, so that the downward depression is about 1500 m. Generally, the mass balance at the glacier surface depends strongly on the elevation of the surface, and adjustment of the bedrock may be expected to have a large effect on the evolution of ice sheets. It is therefore important to include geodynamics in a numerical model that is used to simulate ice-sheet evolution over longer periods of time.

In most models, adjustments of the bed are calculated using a two-layer model for the earth deformation. The outer shell, or lithosphere, consists of rocks that are relatively cool and rigid and that do not deform significantly. The thickness of the lithosphere is about 100 km underneath ocean basins and about 200 km beneath continents. This is small compared with the radius of the earth, so that the lithosphere may be considered a thin elastic plate. Its lower boundary is often defined by the 1600 K isotherm, because rock beneath this isotherm is sufficiently hot for solid-state creep to occur. This lower layer of warm and deforming rock is called the asthenosphere. On geological time scales, the asthenosphere may be considered as a layer of viscous material.

The simplest model for bedrock adjustment is based on the principle of local isostatic equilibrium, illustrated in Figure 9.10. The lithosphere is assumed to be in

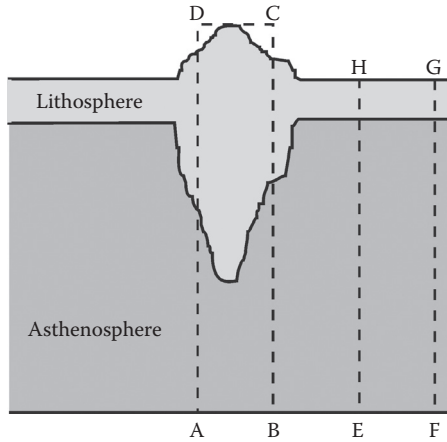


**FIGURE 9.10** Illustration of isostatic equilibrium. The lithosphere under a surface load (mountain) bends downward such that the total mass in a column remains constant. (Reproduced from Oerlemans, J., and C. J. van der Veen, *Ice Sheets and Climate*, Reidel Publishing Co., Dordrecht, 1984. With permission from Springer Verlag.)

floating equilibrium with the underlying heavier substrate in the asthenosphere, and the total mass of a vertical column is constant. Thus, when a mountain or ice sheet is present, the lithosphere (made up of relatively light rock) will bend downward, replacing part of the heavier material in the asthenosphere, such that the total mass of column ABCD equals that of column EFGH. The deflection,  $w$  (taken positive when downward) follows immediately from the thickness of the ice sheet,  $H$ , and the ratio of ice density,  $\rho$ , to that of the substratum,  $\rho_m$

$$w = \frac{\rho}{\rho_m} H \approx \frac{1}{3} H. \quad (9.85)$$

This relation is often used in analytical models that consider the equilibrium profile of ice sheets. However, the deflection is not instantaneous. Because of the viscous flow in the asthenosphere, isostatic equilibrium will be reached after thousands of years. This lagged response introduces an important feedback mechanism. As a start, the delay can be included in a numerical model by calculating bedrock sinking from (Oerlemans, 1980)

$$\frac{\partial b}{\partial t} = -\frac{1}{T_b} \left( \frac{1}{3} H + b - b_0 \right), \quad (9.86)$$

where  $b$  represents the elevation of the bed (negative below sea level) and  $b_0$  the unperturbed bed elevation in the absence of ice.  $T_b$  is a time scale indicating how

fast the system returns to isostatic equilibrium ( $b = b_o - H/3$ ). The value of this time scale strongly influences the behavior of the model ice sheet (Oerlemans, 1980), so it seems worthwhile to use a more realistic model for bedrock adjustment that does not require prescribing the time scale for adjustment. This requires a model for the deflection of the lithosphere that takes into account the elastic properties of this layer, and a model that describes the viscous flow in the asthenosphere.

Deflection of the lithosphere is similar to the bending of a rigid elastic plate subject to a vertical load,  $q$ , and can be calculated from the general equation (c.f. Turcotte and Schubert, 2002, ch. 3)

$$D \nabla^4 w = q - (\rho_m - \rho) g w, \quad (9.87)$$

in which  $w$  represents the deflection, again taken positive when downward, and  $D$  the flexural rigidity of the lithosphere. The second term on the right-hand side represents the upward buoyancy force that arises from the displacement of heavier substratum. This force tends to restore the undisturbed situation ( $w = 0$ ). Equation (9.87) is a linear equation, which means that the *total* deflection of the lithosphere under a surface load can be found by considering the sum of (many) point loads. In a numerical ice-sheet model, the ice thickness is known at discrete gridpoints, and each of these thicknesses may be considered a point load. Calculating the deflection caused by each of these point loads and adding the results gives the total deflection.

Consider first the one-dimensional case in which the ice-sheet profile is computed along a flowline. Equation (9.87) then reduces to

$$D \frac{d^4 w}{dx^4} + (\rho_m - \rho) g w = q(x). \quad (9.88)$$

For a point load,  $Q_i$ , applied at  $x = 0$ , the solution is (Turcotte and Schubert, 2002, p. 125)

$$w_i(x) = \frac{Q_i}{8D} \alpha^3 e^{-\tilde{x}} (\cos \tilde{x} + \sin \tilde{x}), \quad (9.89)$$

where

$$\tilde{x} = \frac{|x|}{\alpha},$$

$$\alpha = \left( \frac{4D}{\rho_m g} \right)^{1/4}. \quad (9.90)$$

This solution is shown in [Figure 9.11](#). An interesting and important feature is the presence of a forebulge at a distance of approximately  $3\alpha$  from the load. This forebulge results from the rigidity of the lithosphere. Observations suggest that the value of  $\alpha$  is about 180 km (Walcott, 1970). With  $\rho_m = 3300 \text{ kg/m}^3$ , this gives  $D = 85 \cdot 10^{24} \text{ Nm}$  for the flexural rigidity of the lithosphere. The value of  $D$  does not greatly influence the actual deflection, but the position of the forebulge is affected by this value.

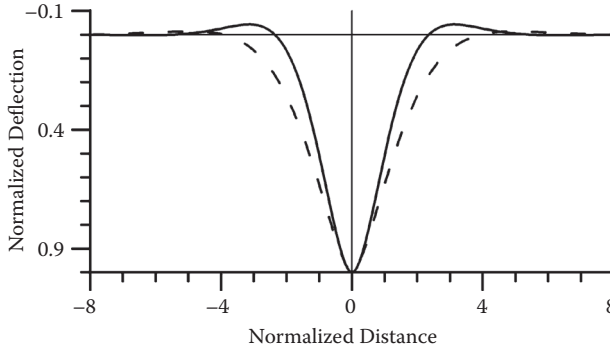


**FIGURE 9.11** Deflection of the lithosphere under a point load applied at  $x = 0$ . The full curve represents the one-dimensional solution (9.89) and the dashed curve the two-dimensional solution (9.95). The deflection is normalized with the deflection directly under the point load, and the horizontal distance is normalized with the flexural length,  $\alpha$ , and radius of relative stiffness,  $L_b$ , respectively.

If the gridpoints are denoted by a subscript  $i$ , the load at a gridpoint with grounded ice is

$$Q_i = \rho g H \Delta x, \quad (9.91)$$

in which  $\Delta x$  represents the grid spacing. If no grounded ice is present and the bed is below sea level, the weight of water (with density  $\rho_w$ ) not present in the undisturbed situation needs to be taken into account. Denoting the actual bed elevation by  $b$ , and the undisturbed elevation by  $b_0$ , this water load is

$$Q_i = \rho_w g (b - b_0). \quad (9.92)$$

For each point load, the corresponding deflection can be calculated from the solution (9.89). The total deflection due to the presence of the entire ice sheet is then

$$w(x) = \sum_{i=1}^I w_i(x). \quad (9.93)$$

In [Figure 9.12](#), the lithospheric deflection under the weight of an ice sheet is shown. Also shown in this figure is the deflection calculated from equation (9.85) for local isostatic adjustment. Differences between the two curves are generally small, except near the margins of the ice sheet. Because the topography near the ice-sheet edge may critically influence the position of the edge, especially in the case of a marine ice sheet grounded below sea level, it seems important to consider the elastic properties of the lithosphere when calculating bedrock adjustment.

For two-dimensional models, in which ice flow in both horizontal directions is considered, flexure of the lithosphere can be calculated in a similar manner as for

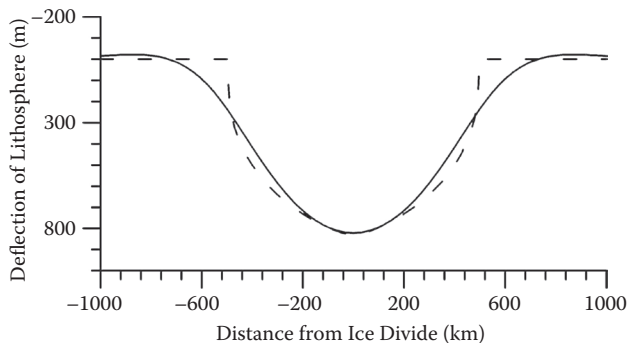


**FIGURE 9.12** Deflection of the lithosphere due to the presence of an ice sheet, for local isostatic equilibrium (dashed curve) and taking into account the rigidity of the lithosphere (solid curve). The dashed curve mirrors the ice-sheet profile divided by a factor of 3. (Reproduced from Oerlemans, J., and C. J. van der Veen, *Ice Sheets and Climate*, Reidel Publishing Co., Dordrecht, 1984. With permission from Springer Verlag.)

the one-dimensional case discussed above. The response of the lithosphere to a point load is axisymmetric, so that equation (9.87) may be written as

$$D \left( \frac{\partial^2 w}{\partial r^2} + \frac{1}{r} \frac{\partial w}{\partial r} \right)^2 + (\rho_m - \rho) g w = q(r), \quad (9.94)$$

in which  $r$  represents the radial distance to the point load. For a point load,  $Q_i$ , applied at  $r = 0$ , the solution is (Brothie and Silvester, 1969)

$$w_i(\tilde{r}) = \frac{Q_i L_b^2}{2\pi D} \text{kei}(\tilde{r}), \quad (9.95)$$

in which

$$\tilde{r} = \frac{r}{L_b}, \quad L_b = \left( \frac{D}{\rho_m g} \right)^{1/4}. \quad (9.96)$$

In this expression,  $L_b$  represents the radius of relative stiffness. For the flexural rigidity estimated above, this length scale is about 130 km. The function  $\text{kei}(\tilde{r})$  denotes the Kelvin function of zero order. This function is tabulated in mathematical handbooks such as Abramowitz and Stegun (1965), who also give polynomial approximations. The dashed line in Figure 9.11 shows the solution (9.95) as a function of normalized distance from the point load; this solution is symmetric around the vertical at the origin ( $r = 0$ ). The total lithospheric deflection under an ice sheet is again found by summation of all deflection from point loads at the grid nodes.

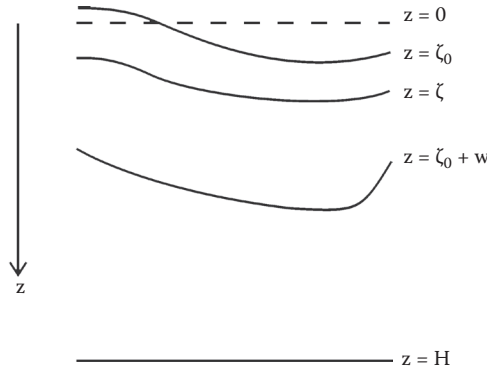


**FIGURE 9.13** Geometry used in the derivation of the equation for the rate of bedrock adjustment. Note that the vertical coordinate,  $z$ , is positive downward. (Reproduced from Oerlemans, J., and C. J. van der Veen, *Ice Sheets and Climate*, Reidel Publishing Co., Dordrecht, 1984. With permission from Springer Verlag.)

The flexure of the lithosphere controls the equilibrium bedrock adjustment. The rate at which this equilibrium is achieved is controlled by the viscous properties of the asthenosphere. Flow in this layer is induced by pressures exerted by the lithosphere. Similar to the model for viscous flow of subglacial till, described in Section 7.3, the equation of motion in the asthenosphere is (compare equation (7.44) with  $\theta = 0$ )

$$\frac{\partial^2 u}{\partial z^2} = \frac{1}{\eta} \frac{\partial P}{\partial x}, \quad (9.97)$$

in which  $u$  represents the horizontal component of velocity in the asthenosphere and  $\eta$  the viscosity. The geometry is shown in Figure 9.13. As reference level,  $z = 0$  is chosen;  $z = \zeta_0$  denotes the unperturbed upper boundary of the asthenosphere and  $z = \zeta$  the actual upper boundary. The lower boundary is at  $z = H$ , although this is a rather artificial boundary needed in the following derivation. Note that  $z$  is taken positive in the downward direction.

Flow in the asthenosphere will start when the lithosphere deflects downward and will cease when full adjustment to the ice load is achieved. Because deflection of the lithosphere displaces the upper boundary of the asthenosphere, the pressure,  $P$ , driving the flow may be written as

$$P = \rho_m g(\zeta_0 - \zeta + w). \quad (9.98)$$

Equation (9.97) can now be integrated twice with respect to  $z$  to yield the velocity profile

$$u(z) = \frac{g}{2\eta}(z^2 - 2Hz) \frac{\partial}{\partial x}(\zeta_0 - \zeta + w). \quad (9.99)$$



In deriving this expression, the following boundary conditions are used:

$$\begin{aligned} u &= 0 \quad \text{at} \quad z = \zeta, \\ \frac{\partial u}{\partial z} &= 0 \quad \text{at} \quad z = H. \end{aligned} \quad (9.100)$$

The second boundary condition states that the asthenosphere does not exert a stress on the underlying material.

Considering a vertical column extending from  $z = \zeta$  to  $z = H$ , conservation of mass requires

$$\frac{\partial \zeta}{\partial t} = -\frac{\partial}{\partial x} \int_{\zeta}^H u \, dz. \quad (9.101)$$

The integral is approximated as

$$\int_{\zeta}^H u \, dz \approx \int_0^H u \, dz. \quad (9.102)$$

Substituting the velocity profile (9.99) and calculating the integral gives

$$\frac{\partial \zeta}{\partial t} = \frac{gH^3}{3\eta} \frac{\partial^2}{\partial x^2} (\zeta_0 - \zeta + w). \quad (9.103)$$

If the lower boundary  $z = H$  remains fixed, this equation describes how the thickness of the asthenosphere evolves. This thickness determines directly the depression of the bedrock under the ice (since the thickness of the lithosphere is assumed constant), so the rate of change of bedrock elevation is given by

$$\frac{\partial b}{\partial t} = \frac{gH^3}{3\eta} \frac{\partial^2}{\partial x^2} (b_0 - b + w). \quad (9.104)$$

For the two-dimensional case, a similar equation that includes flow in the other horizontal direction can be used.

The rate of bedrock adjustment is governed by the diffusion equation (9.104). The characteristic time scale for adjustment is

$$T_b = \frac{3\eta L^2}{gH^3}, \quad (9.105)$$

in which  $L$  represents the length scale of the load. This expression shows that  $T_b$  increases with the size of the ice sheet above. For small ice sheets, adjustment occurs relatively rapidly, but for large ice sheets, adjustment may take up to tens

of thousands of years. This means that the earth's crust is still adjusting after the Northern Hemisphere glacial ice sheets disappeared some 10,000 years ago.

The diffusivity of the asthenosphere is

$$D_a = \frac{gH^3}{3\eta}. \quad (9.106)$$

Neither the thickness,  $H$ , nor the viscosity,  $\eta$ , of the asthenosphere is known. However,  $D_a$  can be estimated from measurements of glacial uplift. Walcott (1970) calculates a range for  $D_a$  from 35 to 50 km<sup>2</sup>/yr, based on observations in North America and Scandinavia. The results of coupled ice-flow and geodynamics models are rather insensitive to the particular choice of  $D_a$ , and of the flexural rigidity of the lithosphere,  $D$ , as well. This is probably because the equations that describe geodynamics in the present model are linear. This linearity also suggests that results will be similar for the two-dimensional case.

After bedrock adjustment has reached equilibrium, the height of the forebulge is rather small, about 4% of the depression under the center of the ice sheet (Figure 9.12). However, while the ice sheet is forming, this height may be considerably larger. This is shown in Figure 9.14 for an ice sheet that, after reaching equilibrium, is about 4000 m thick and has a half-width of about 500 km. The forebulge reaches a maximum height of about 240 m and subsequently decreases in size to the equilibrium value of about 15 m. This transient behavior is caused by the diffusive character of the flow in the asthenosphere. While the ice sheet is building up, its weight causes the substratum to spread horizontally, away from directly under the ice sheet. Because the flow is highly viscous, it takes a long time before the surrounding substratum starts to move out as well. As a result, material in the asthenosphere will initially pile up near the edge of the ice sheet until local pressure gradients are sufficiently large to drive this excess substratum farther out. Similarly, when the ice sheet melts away in a short period of time, the bedrock in the vicinity of the edge will sink a few

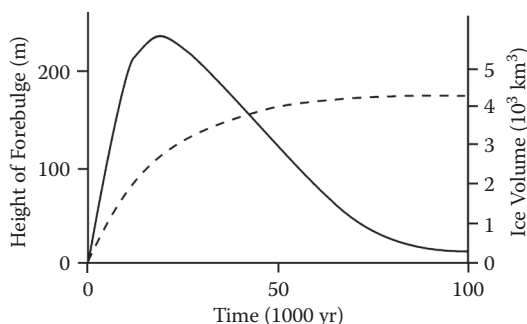


**FIGURE 9.14** Growth and decay of the forebulge (solid line) when an ice sheet is building up to equilibrium. The dashed line gives the ice volume. (Reproduced from Oerlemans, J., and C. J. van der Veen, *Ice Sheets and Climate*, Reidel Publishing Co., Dordrecht, 1984. With permission from Springer Verlag.)

hundred meters, while the bedrock under the central part of the (former) ice sheet rises immediately.

The model for bedrock adjustment described above assumes that the lithosphere is continuous, with constant elastic properties. Stern and Ten Brink (1989) argue that this may not be appropriate for the Antarctic shield. They suggest that East and West Antarctica should be considered separately, with free edges at their common boundary (the Transantarctic Mountains). Applying this model results in smaller lithospheric deflection in the Transantarctic Mountains. Stern and Ten Brink (1989) also argue that the flexural rigidity may be much smaller for the Ross Embayment than the estimate given above. This would make bedrock adjustments more local in this region.

Other models have been proposed to describe adjustment of the bedrock under ice sheets (Lambeck and Nakiboglu, 1981; Lingle and Clark, 1985; Peltier, 1982, 1985, 1987). Peltier and Hyde (1987) argue that the time scale for adjustment in the viscous model (about 10,000 yr) is in sharp discord with geophysical constraints. Peltier (1985, 1988) suggests that the modeled transient forebulge may not be realistic, based on a comparison of modeled postglacial rebound with observed records of relative sea level. The problem is that the rheology of the asthenosphere cannot be measured directly, of course, but must be inferred from records of past sea-level stands (indicating postglacial rebound) and changes in ice volume. While the decrease in the total volume of ice stored on the earth during the last deglaciation can be estimated with reasonable accuracy, it is not clear which ice sheets contributed to the following rapid rise in sea level. In particular, the contribution from the West Antarctic Ice Sheet is, as of yet, disputed. Given the considerable uncertainty concerning the location and timing of the (un)loading of the lithosphere by the large ice sheets, inferring the viscous properties of the asthenosphere and deducing the most appropriate rheological model remains speculative. It is not immediately clear, however, that more advanced models for bedrock adjustment will significantly alter the modeled behavior of ice sheets.

## 9.7 ICE-SHELF MODELS

On floating ice shelves, basal drag is zero and the driving stress is balanced by gradients in longitudinal stress and by lateral drag. As a start, one-dimensional flow along the centerline of an ice shelf is considered, with the  $x$ -axis along the direction of flow. The balance of forces for this case is discussed in Section 4.5 where the following balance equation (4.68) is derived.

$$\frac{\partial}{\partial x}(\mathbf{H}\mathbf{R}_{xx}) = \frac{1}{2}\rho g \left(1 - \frac{\rho}{\rho_w}\right) \frac{\partial \mathbf{H}^2}{\partial x} - \frac{\mathbf{H}\tau_s}{W}. \quad (9.107)$$

In this expression,  $\rho$  and  $\rho_w$  represent the density of ice and sea water, respectively. The second term on the right-hand side describes resistance to flow from lateral drag originating at the margins if the ice shelf is laterally confined. The assumption is made that the lateral shearing stress,  $\mathbf{R}_{xy}$ , varies linearly across the width of the ice shelf, meaning that lateral drag supports the same fraction of driving stress across the full width. The shear stress at the margins,  $\tau_s$ , is taken constant for now.

Integrating the balance equation (9.107) from the ice-shelf front (at  $x = L$ ) to some distance  $L - x$  upglacier gives

$$R_{xx} = \frac{1}{2} \rho g \left( 1 - \frac{\rho}{\rho_w} \right) H - \frac{1}{H} \int_x^L \frac{H \tau_s}{W} d\bar{x}. \quad (9.108)$$

This expression allows the resistive stress,  $R_{xx}$ , to be calculated along the entire ice shelf. Invoking the constitutive relation (4.62), the stretching rate, and thus the along-flow gradient in ice velocity can then be calculated. If the ice velocity at the grounding line is known, the velocity on the ice shelf can be found from

$$U = \int_0^x \dot{\epsilon}_{xx} d\bar{x} + U_0, \quad (9.109)$$

in which  $U_0$  represents the ice velocity at the grounding line.

The expressions given above show that the ice-shelf model is essentially different from the ice-sheet model discussed in Section 9.3. For lamellar flow, the driving stress is balanced by drag at the glacier bed, and the ice flux can be calculated from the local geometry (equation (9.28)). The ice-shelf model, on the other hand, requires two integrations along the entire ice shelf. The first integration, starting at the ice-shelf front, yields the resistive normal stress,  $R_{xx}$ , and the second integration, starting at the grounding line, gives the velocity,  $U$ .

With the velocities and stretching rate known along the entire ice shelf, the time evolution can be calculated from the continuity equation, written in the form similar to equation (5.67):

$$\frac{\partial H}{\partial t} = -U \frac{\partial H}{\partial x} - H \dot{\epsilon}_{xx} + M. \quad (9.110)$$

Using a forward-in-time numerical scheme, this equation is readily solved. If the ice shelf front is advancing, a new grid needs to be defined at the start of each time step. Given the velocity at the last gridpoint, the new length of the ice shelf can be calculated and a new grid defined. The ice-shelf profile is then transferred from the old to the new grid, and thickness changes calculated at each of the new gridpoints. The thickness at the last gridpoint follows from conservation of mass, but with the restriction that this thickness cannot be larger than that of the gridpoint located just upstream. The time step must be chosen sufficiently small so that there is only one point on the new grid (namely, the last point) where at the beginning of the time step no ice is present. To prevent the ice shelf from becoming unrealistically large, either a critical minimum thickness can be specified or the maximum length of the ice shelf may be prescribed. Alternatively, a more realistic calving criterion (Section 8.5) can be prescribed.

Figure 9.15 shows an equilibrium profile calculated with the model described above. Also shown in this figure is the steady-state solution (5.77) derived in Section 5.5. The thickness and velocity at the grounding line are prescribed and kept constant

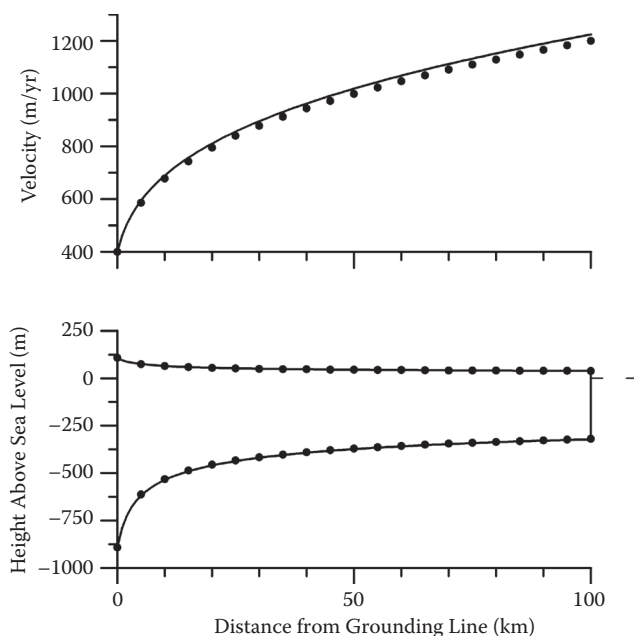


**FIGURE 9.15** Equilibrium profile of an unconfined ice shelf as calculated with the numerical flowline model. Dots represent the analytical solution (5.77).

(at 1000 m and 400 m/yr, respectively), while the maximum length is set to 100 km. The velocity calculated with the time-evolving model is somewhat larger than that predicted by the analytical solution, which results in a slightly thicker ice shelf, although differences between the two profiles are undistinguishable in the lower panel of Figure 9.15. Because the velocity is determined by integrating the stretching rate along the centerline, the grid spacing needs to be small (1 km in the example shown here); if the spacing is too large, velocities are overestimated, especially near the grounding line where the stretching rate decreases rapidly in the direction of flow. By replacing the central difference approximation for the gradient in ice velocity with a more sophisticated numerical scheme, this effect could perhaps be avoided.

Including lateral drag has a large effect on the ice shelf. Figure 9.16 shows the steady-state profile of a 20 km wide ice shelf with a shear stress of 100 kPa acting at its lateral margins. The resistance offered by lateral drag allows the shelf to become considerably thicker, while the ice velocity is much smaller (so that the ice flux is the same as for the free-floating case).

The model described above was used by Van der Veen (1986) to investigate some properties of ice-shelf spreading and, in particular, the response of ice shelves to changes at the grounding line. A more elaborate version that includes calculation of the temperature field was applied by Lingle et al. (1991) to a flowband on the Ross Ice Shelf, to assess the response of this ice shelf to a CO<sub>2</sub>-induced climatic warming. In both models, the ice speed is calculated from the stretching rate. However, this may not be entirely realistic for the Antarctic ice shelves. Measurements of velocity on the

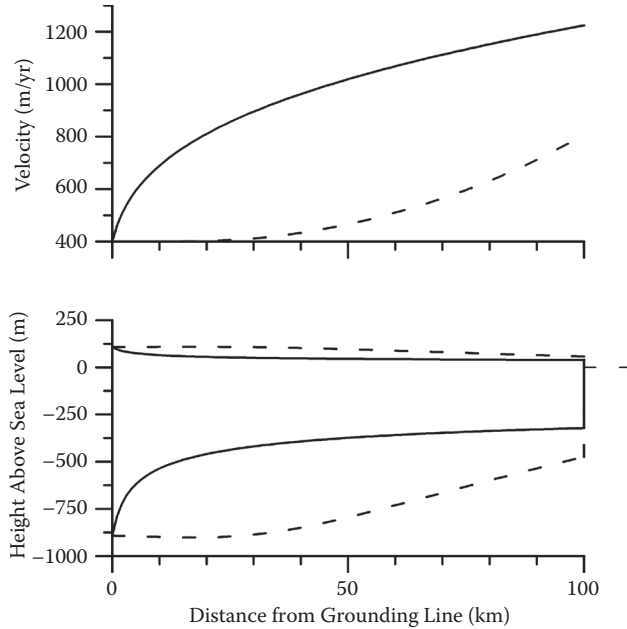


**FIGURE 9.16** Effect of lateral drag on the equilibrium profile of an ice shelf. The solid profile is that of an unconfined ice shelf, while the dashed profile represents the equilibrium profile of an ice shelf with a total width of 20 km subject to a shear stress at the margins of 100 kPa.

Ross Ice Shelf suggest that the driving stress is mostly balanced by lateral drag, with gradients in longitudinal stress being small (Thomas and MacAyeal, 1982; Whillans and Van der Veen, 1993b). This suggests that the stretching rate may not be the best quantity to use for estimating the velocity of the ice shelf. Rather, the velocity should be calculated from lateral drag and balance of forces.

If the driving stress is fully supported by drag at the margins, the model developed in Section 5.6 can be used. The numerical scheme for solving the continuity equation for time evolution of the ice shelf is analogous to the scheme discussed in Section 9.3. Again, the ice flux is proportional to the local surface slope, allowing the continuity equation to be written as a diffusion equation, with diffusivity (from equation (5.90))

$$D = \frac{2AH}{n+2} W^{n+1} (\rho g)^n \left| \frac{\partial h}{\partial x} \right|^{n-1}. \quad (9.111)$$

An example of a steady-state profile calculated with this model is shown in Figure 9.17. The width of the ice shelf is 30 km. As boundary condition, the ice thickness as well as the ice velocity at the grounding line are prescribed, to make the model comparable to the ice-shelf model discussed previously. Because the ice velocity is linked to the driving stress, these boundary conditions implicitly prescribe the surface slope at

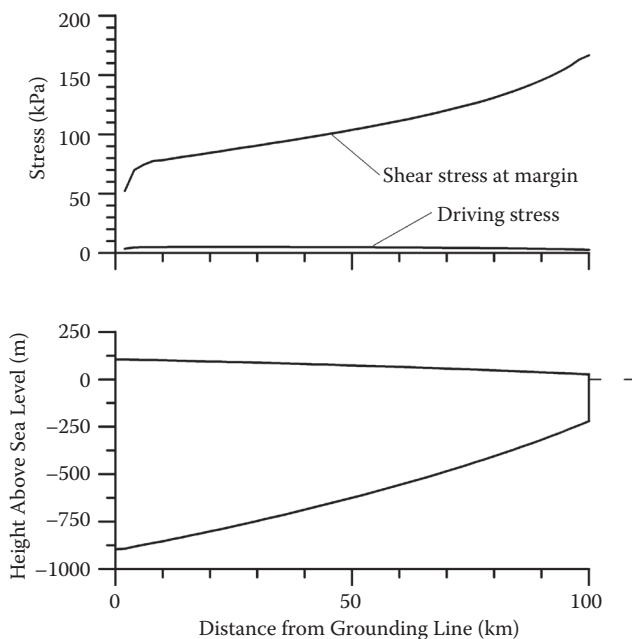


**FIGURE 9.17** Equilibrium profile of an ice shelf on which the driving stress is balanced entirely by lateral drag. The total width of the ice shelf is 30 km.

the grounding line as well. This allows the diffusivity at the grounding line (needed to calculate the ice flux at the first intermediate gridpoint) to be calculated.

Contrary to the lamellar flow model described in Section 9.3, ice shelf models are not readily extended to include both horizontal dimensions. This is because resistance to flow from lateral drag or gradients in longitudinal stress is linked to spatial gradients in resistive stresses. This means that the balance equations must be solved by numerical iteration.

Vertical shear is small on ice shelves (Sanderson and Doake, 1979), and horizontal strain rates may be taken constant with depth. With basal drag zero under floating ice shelves, the force-balance equations derived in Section 3.1 become

$$\tau_{dx} = -\frac{\partial}{\partial x}(HR_{xx}) - \frac{\partial}{\partial y}(HR_{xy}), \quad (9.112)$$

and

$$\tau_{dy} = -\frac{\partial}{\partial x}(HR_{xy}) - \frac{\partial}{\partial y}(HR_{yy}). \quad (9.113)$$

Using the constitutive relation, the horizontal resistive stresses can be expressed in terms of strain rates (Section 3.3). The weight of an ice shelf is fully supported by the

water below, so bridging effects may be neglected. Rewriting the balance equations in terms of velocity gradients gives

$$\frac{\tau_{dx}}{B} = -\frac{\partial}{\partial x} \left( H \dot{\epsilon}_e^{1/n-1} \left( 2 \frac{\partial U}{\partial x} + \frac{\partial V}{\partial y} \right) \right) - \frac{\partial}{\partial y} \left( H \dot{\epsilon}_e^{1/n-1} \frac{1}{2} \left( \frac{\partial U}{\partial y} + \frac{\partial V}{\partial x} \right) \right), \quad (9.114)$$

and

$$\frac{\tau_{dy}}{B} = -\frac{\partial}{\partial x} \left( H \dot{\epsilon}_e^{1/n-1} \frac{1}{2} \left( \frac{\partial U}{\partial y} + \frac{\partial V}{\partial x} \right) \right) - \frac{\partial}{\partial y} \left( H \dot{\epsilon}_e^{1/n-1} \left( \frac{\partial U}{\partial x} + 2 \frac{\partial V}{\partial y} \right) \right). \quad (9.115)$$

The effective strain rate is given by

$$\dot{\epsilon}_e^2 = \frac{1}{2} \left( \frac{\partial U}{\partial x} \right)^2 + \frac{1}{2} \left( \frac{\partial V}{\partial y} \right)^2 + \frac{1}{4} \left( \frac{\partial U}{\partial y} + \frac{\partial V}{\partial x} \right)^2. \quad (9.116)$$

In these expressions,  $U$  and  $V$  represent the components of velocity in the horizontal  $x$ - and  $y$ -directions, respectively.

Huybrechts (1992) uses the point relaxation technique to solve this set of coupled equations for the two components of velocity. Following his notation, the equations are formally written as

$$a_{i,j} U_{i,j} + c_{i,j} = 0, \quad (9.117)$$

and

$$b_{i,j} V_{i,j} + d_{i,j} = 0, \quad (9.118)$$

where the subscripts  $i$  and  $j$  refer to the gridpoint coordinates. The coefficients  $a_{i,j}$ ,  $b_{i,j}$ ,  $c_{i,j}$ , and  $d_{i,j}$  are functions of the driving stress, effective strain rate, and velocities at neighboring gridpoints (c.f. Huybrechts, 1992, for the respective formulas). The neighboring velocities enter into these coefficients after approximating the gradients by central differences. The numerical solution starts with a guess for the two components of velocity and determining the local residuals

$$R(U_{i,j}^{(1)}) = a_{i,j}^{(1)} U_{i,j}^{(1)} + c_{i,j}^{(1)}, \quad (9.119)$$

$$R(V_{i,j}^{(1)}) = b_{i,j}^{(1)} V_{i,j}^{(1)} + d_{i,j}^{(1)}. \quad (9.120)$$

Here, the superscript refers to the iteration step. The next guess for the velocities is

$$U_{i,j}^{(2)} = U_{i,j}^{(1)} - \frac{R(U_{i,j}^{(1)})}{a_{i,j}^{(1)}}, \quad (9.121)$$

$$V_{i,j}^{(2)} = V_{i,j}^{(1)} - \frac{R(V_{i,j}^{(1)})}{b_{i,j}^{(1)}}. \quad (9.122)$$



If the coefficients were independent of the values at the surrounding gridpoints, the residuals would now be zero. However, because the new velocities affect calculations at the surrounding gridpoints, the procedure has to be repeated until the maximum residual on the grid is sufficiently small. According to Huybrechts (1992), convergence occurs rather slowly, and initially requires a few thousand iteration steps, starting with zero velocities everywhere.

This two-dimensional solution scheme for ice-shelf flow does not allow the continuity equation to be written as a diffusion equation. The ice flux is directly calculated from the ice velocities and ice thickness. This tends to make the solution unstable and may lead to (initially) small-amplitude oscillations in calculated ice thickness. To avoid these oscillations, Huybrechts (1992) applies spatial smoothing. The thickness at each gridpoint is set equal to the average thickness over a nine-grid square, assigning a 5% weight to the values at the eight surrounding gridpoints.

Determann (1991) applies a model similar to that of Huybrechts (1992) to simulate the flow of the Ronne-Filchner Ice Shelf in West Antarctica. The present-day ice thickness is prescribed, with the calving front held fixed at the current average position. At this front, the stretching rate is prescribed from solution (4.65) for an ice shelf spreading freely in both horizontal directions. Along the remaining ice-shelf margins, including around ice rises, the velocity parallel to the margin is set to zero except where the ice shelf is nourished by ice streams; for these ice streams, the width and mass flux across the grounding line are prescribed.

Special treatment is needed for ice rises and ice rumpled where the ice shelf has run aground. These obstructions to flow affect the spreading rate and hence the velocity of the ice shelf. Ice rises can reach elevations of several hundred meters above the surrounding ice shelf and may be considered decoupled from the ice shelf. Zero velocity along their margins can be prescribed if the small amount of ice flowing outward into the surrounding shelf ice is ignored. Ice rumpled, on the other hand, are more subtle features with surface elevations up to about 30 m higher than the surrounding ice. The most prominent rumpled on the Ronne-Filchner Ice Shelf are the Doake Ice Rumpled between Korff and Henry Ice Rises. While these rumpled obstruct the flow due to local basal drag, the ice there forms an integral part of the ice shelf. Ideally, a full calculation of stresses around these obstacles should be included in the model, but this is not well feasible. Instead, Determann (1991) includes the effect of ice rumpled in a parameterized way. Defining the height above buoyancy as

$$H_b = H - \frac{\rho_w}{\rho} D, \quad (9.123)$$

in which  $D$  represents the water depth, a correction factor

$$r = 1 - \frac{H_b}{30}, \quad H_b < 30 \text{ m}, \quad (9.124)$$

is applied to the two components of driving stress in the force-balance equations (9.114) and (9.115). If the height above buoyancy is greater than 30 m, the driving stress is zero and the obstruction is considered an ice rise with zero ice velocity. For  $H_b = 0$ , the correction factor is zero, corresponding to a free-spreading ice shelf.

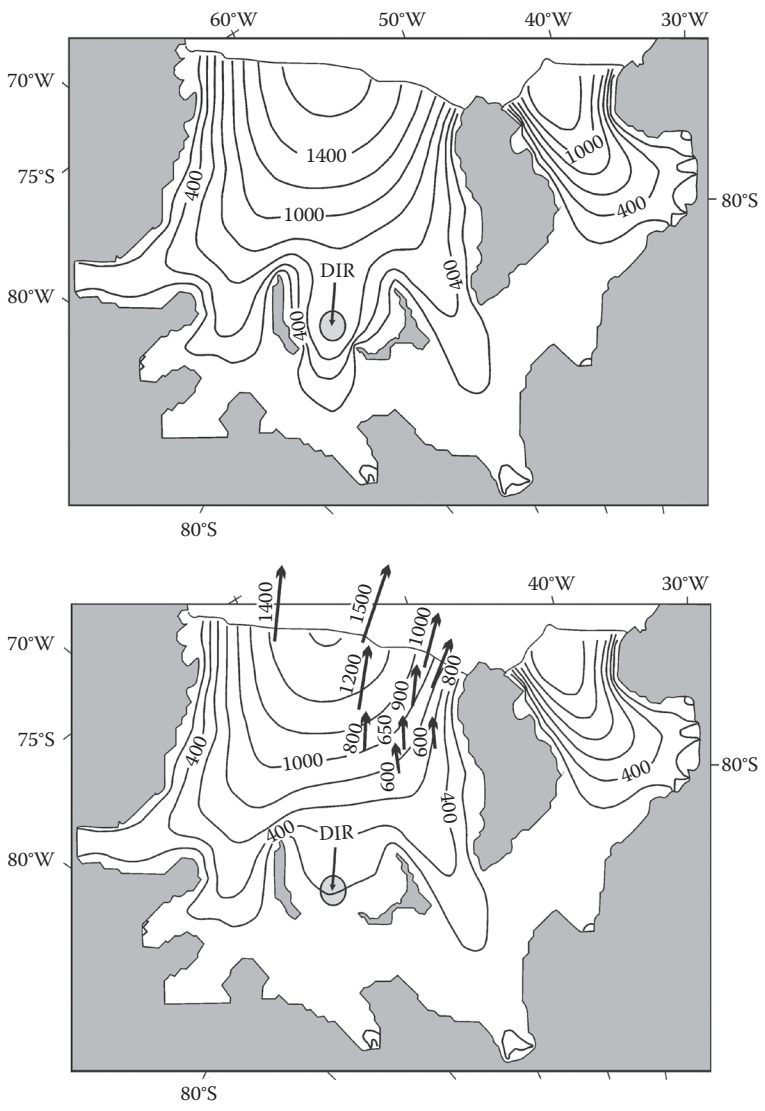


**FIGURE 9.18** Contours of calculated ice velocity (interval: 200 m) on the Ronne–Filchner Ice Shelf. The upper panel is the result of a calculation that does not include the effect of the Doake Ice Rumples (DIR) on ice flow, while the lower panel is based on a calculation that accounts for these effects by lowering the local driving stress. Arrows in the lower panel represent observed velocities. (From Determann, J., *Ber. Polarforsch.*, 83, 1991.)

Figure 9.18 shows the effect of the ice rumples (indicated by DIR between the two ice rises) on the simulated flow of the ice shelf. If the obstructing effect of the rumples is not included, local speeds in excess of 800 m/yr are reached. Near the calving front of the Ronne Ice Shelf, velocities become greater than 1600 m/yr, compared with 1200 m/yr on the Filchner Ice Shelf. Including the slowing effect of the

ice rumples eliminates the local velocity maximum between the two ice rises and also results in somewhat lower velocities downstream; the Filchner Ice Shelf is unaffected by these changes. The resulting velocity distribution agrees reasonably with measured speeds (indicated by the arrows in the panel on the right). Determann (1991) also conducts time-evolving calculations of the ice-shelf profile to investigate the sensitivity of the ice shelf to changes in surface accumulation and basal melting rates. As expected, interaction with the ocean through basal melting has the largest effect on the shelf thickness (as also concluded from the equilibrium profiles derived in Section 5.5; c.f. Figure 5.11).

Vieli et al. (2006) use observed velocities on the Larsen B Ice Shelf in the Antarctic Peninsula to constrain a two-dimensional ice-shelf model (equations (9.114)–(9.116)) and infer the spatial distribution of the viscosity parameter,  $B$ . They find strong weakening of ice in shear zones along the margins and suggest that these weak zones play a major role in controlling the flow of this ice shelf. Subsequent perturbation modeling experiments indicate that the acceleration of the Larsen B Ice Shelf prior to its collapse in 2002 may have resulted from further significant weakening of the already weak shear zones within the ice shelf (Vieli et al., 2007).

